INFORMATION TO USERS

This manuscript has been reproduced from the microfilm master. UMI films the text directly from the original or copy submitted. Thus, some thesis and dissertation copies are in typewriter face, while others may be from any type of computer printer.

The quality of this reproduction is dependent upon the quality of the copy submitted. Broken or indistinct print, colored or poor quality illustrations and photographs, print bleedthrough, substandard margins, and improper alignment can adversely affect reproduction.

In the unlikely event that the author did not send UMI a complete manuscript and there are missing pages, these will be noted. Also, if unauthorized copyright material had to be removed, a note will indicate the deletion.

Oversize materials (e.g., maps, drawings, charts) are reproduced by sectioning the original, beginning at the upper left-hand corner and continuing from left to right in equal sections with small overlaps.

Photographs included in the original manuscript have been reproduced xerographically in this copy. Higher quality 6" x 9" black and white photographic prints are available for any photographs or illustrations appearing in this copy for an additional charge. Contact UMI directly to order.

ProQuest Information and Learning
300 North Zeeb Road, Ann Arbor, MI 48106-1346 USA
800-521-0600

Optical Properties and Energy Transfer between C_{3i} and C_2 Sites of Eu^{3+} ions in Y_2O_3 Nanocrystal and Bulk Systems

Tania D'Alesio

A Thesis

in

The Department

of

Chemistry and Biochemistry

Presented in Partial Fulfillment of the Requirements
for the Degree of Master of Science at
Concordia University
Montreal, Quebec, Canada

December 2001

ABSTRACT

Optical Properties and Energy Transfer between C_{3i} and C_2 Sites of Eu^{3+} ions in Y_2O_3 Nanocrystal and Bulk Systems

Tania D'Alesio

Interest in doped nanocrystals is fueled by their potential as efficient phosphors in display and opto-electronic applications since they possess enhanced optical properties. The search for new phosphors has led to the preparation of various forms of lanthanide-doped oxides, such as Eu^{3+} doped Y_2O_3, which exhibits a narrow emission line in the red at ~611nm. Cubic Y_2O_3 forms at high temperature with Y^{3+} ions occupying C_2 and C_{3i} sites, where the C_{3i} site has an inversion center. The effect of two distinct crystallographic sites on the optical properties and energy transfer process between Eu^{3+} ions in a Y_2O_3 lattice has been a recent focus of research in our laboratory.

The luminescence and site selective emission resulting from the direct excitation of the $^5D_0 \rightarrow {}^7F_0$ level of C_2 and the $^5D_0 \rightarrow {}^7F_{1a}$ level of C_{3i} sites at 580.0 and 582.2 nm respectively for Eu^{3+} doped Y_2O_3 nanocrystalline and bulk samples are reported in this thesis. It was observed for the 1mol% nanocrystalline and bulk samples that a two-way energy transfer process becomes possible over a $90cm^{-1}$ energy gap between the $^5D_0$ levels of the distinct sites through thermal bridging at room temperature. The reverse energy transfer process from $C_2 \rightarrow C_{3i}$ sites was observed to decrease in efficiency below 150K as shown by the temperature dependence results.

Furthermore, the investigation of the lifetime of the $^5D_0 \rightarrow {}^7F_2(C_2)$ level for the nanocrystalline and bulk samples confirmed the two-way energy transfer process between $Eu^{3+}(C_{3i}) \leftrightarrow Eu^{3+}(C_2)$ ions since the lifetimes obtained for $^5D_0 \rightarrow {}^7F_2$ level lengthened upon C_{3i} excitation both at 298K and 77K.

ACKNOWLEDGEMENTS

I would like to thank my research supervisor, Dr. J.A. Capobianco for his assistance and guidance in the undertaking of this study.

I would like to thank my committee members, Dr. Georges Dénès and Dr. Timothy A. Gadosy for their commitment to this thesis.

I would like to thank Dr. Narinder Kapoor and for his assistance in conducing the SEM work presented in this thesis. I would also like to express my gratitude to Dr. Georges Dénès and Muntasar Abdualhafed for their wisdom and patience in teaching me the art of X-ray diffraction.

I would like to thank Dr. Marco Bettinelli and Dr. Adolfo Speghini for their skilled work in preparing the samples used in this thesis and for their intuition and guidance from Verona, Italy.

I would like to extend a special thank you to my best friend and colleague, Carmela Mancuso for sharing her remarkable intelligence and allowing me the honour of working alongside her. I would like to thank Elham Ghobadi for her kindness and encouragement during the past two years, which will never be forgotten.

I would like to thank my family for their enduring support, patience and love during challenging times. Thank you Mamma, Angelo, and Nonna Maria for seeing this with me to the end.

Last, but especially not least, I would like to thank my husband Nicholas Xydis for his unconditional love, support and understanding. Most of all, I thank him for not allowing me to give up. I am forever indebted.

To my Loving Husband Nicholas Xydis

TABLE OF CONTENTS

CHAPTER 3

CHAPTER 4

CHAPTER 5

LIST OF FIGURES

LIST OF TABLES

CHAPTER 1

1. INTRODUCTION

1.1 RARE EARTH SPECTROSCOPY

The rare earths, or otherwise known as the lanthanides, form the group of fifteen elements from atomic numbers 57 through 71 in the periodic table, where the successive filling of the $4f$ electronic subshell is carried out by starting from La ($4f^{0}$) to Lu ($4f^{14}$). The neutral atoms have a ground state electronic configuration of a Xe core ($1s^2 2s^2 2p^6 3s^2 3p^6 3d^{10} 4s^2 4p^6 4d^{10} 5s^2 5p^6$) with two or three outer electrons ($6s^2$ or $5d^1 6s^2$) and a number of 4f electrons varying from 0 to 14. Their most common oxidation state is +3, having lost their 5d and 6s electrons leaving the Ce^{3+} through Lu^{3+} ions with the following ground state electronic configuration: [Xe] $4f^{n}$ $5s^2 5p^6$.

Lanthanides are electropositive and their chemistry is primarily ionic where the strength of their electrostatic interactions is determined by the size of the M^{3+} ion [1]. The lanthanide series is often associated with the term: "lanthanide contraction", implying a significant steady decrease in the atomic radii with increasing atomic number. The increase in effective nuclear charge from left to right within the lanthanide series causes an "irregular" reduction in size within the $4f^{n}$ shell. This contraction gives rise to the unique spectroscopic properties observed for the lanthanide series [2]. All lanthanides form the most stable M^{3+} state, while some form the less frequent M^{2+}, and M^{4+} states.

Europium, assigned the atomic number 63, belongs to the lanthanide series that includes the 14 rare earth elements following Lanthanum in the periodic table. The ground state electronic configuration for the Eu^{3+} is the following:

$$1s^2\ 2s^2\ 2p^6\ 3s^2\ 3p^6\ 3d^{10}\ 4s^2\ 4p^6\ 4d^{10}\ 4f^6\ 5s^2\ 5p^6$$

The spectral properties of the lanthanides are different from the transition elements within the d-block. Contrary to transition elements, the *4f* electrons are more effectively shielded from external forces by overlapping of the $5s^2$ and $5p^6$ shells. Thus, the transition states involved with the various *4f* configurations are only slightly affected by their surrounding environment. These differences account for the sharp spectral bands observed for the transitions of rare earth ions in comparison to the broad spectral bands observed for the transition metals [2].

The interpretation of rare-earth spectra was made possible by the theoretical work of Bethe [3] and Kramer [4]. Bethe's work focused on the development of crystal field theory, while Kramer showed that in an odd electron system; every level must remain at least doubly degenerate known as "Kramer's degeneracy". An externally applied magnetic field can remove the degeneracy of these levels. Further work by Spedding et al. [5-7] on the systematic investigation of rare earth spectra confirmed that there were groups of lines clustered closely together (i.e. hundreds of cm^{-1}) separated by larger intervals (i.e. thousands of cm^{-1}). From their work, Freed and Speeding [5] proposed energy level diagrams without realizing that the sharp lines in the spectra were due to

intra 4*f*-configurational transitions. At the time they suggested that the transitions involved were of the 4f→5d or 6s type. Later, the combined work of Van Fleck [8] and Broer et al. [9] was used to construct a simple method of classifying and identifying energy levels split by the crystal field.

Following the development of paramagnetic resonance techniques, Elliot and Stevens were able to obtain more accurate data for the ground state crystal splitting [10,11]. Their work lead to the development of the "Stevens operator equivalents method", which assumes that the perturbations due to the crystal field are small in comparison to the spin orbit coupling which allows the ground state to be considered as an isolated multiplet of constant J. This assumption is valid when the separations between J-levels are larger than the crystal field splitting. However, in the presence of strong crystal fields, where the free ion levels are mixed, the assumption is no longer valid and J-mixing must be included. As a consequence, Judd and Margolis, and Axe and Dieke [7,8,12] included J-mixing in their calculations. Dieke's work is summarized in Figure 1.1.1. The thickness of each level represents the total crystal field splitting in $LaCl_3$. A pendant semicircle indicates that this level fluoresces in the $LaCl_3$ structure.

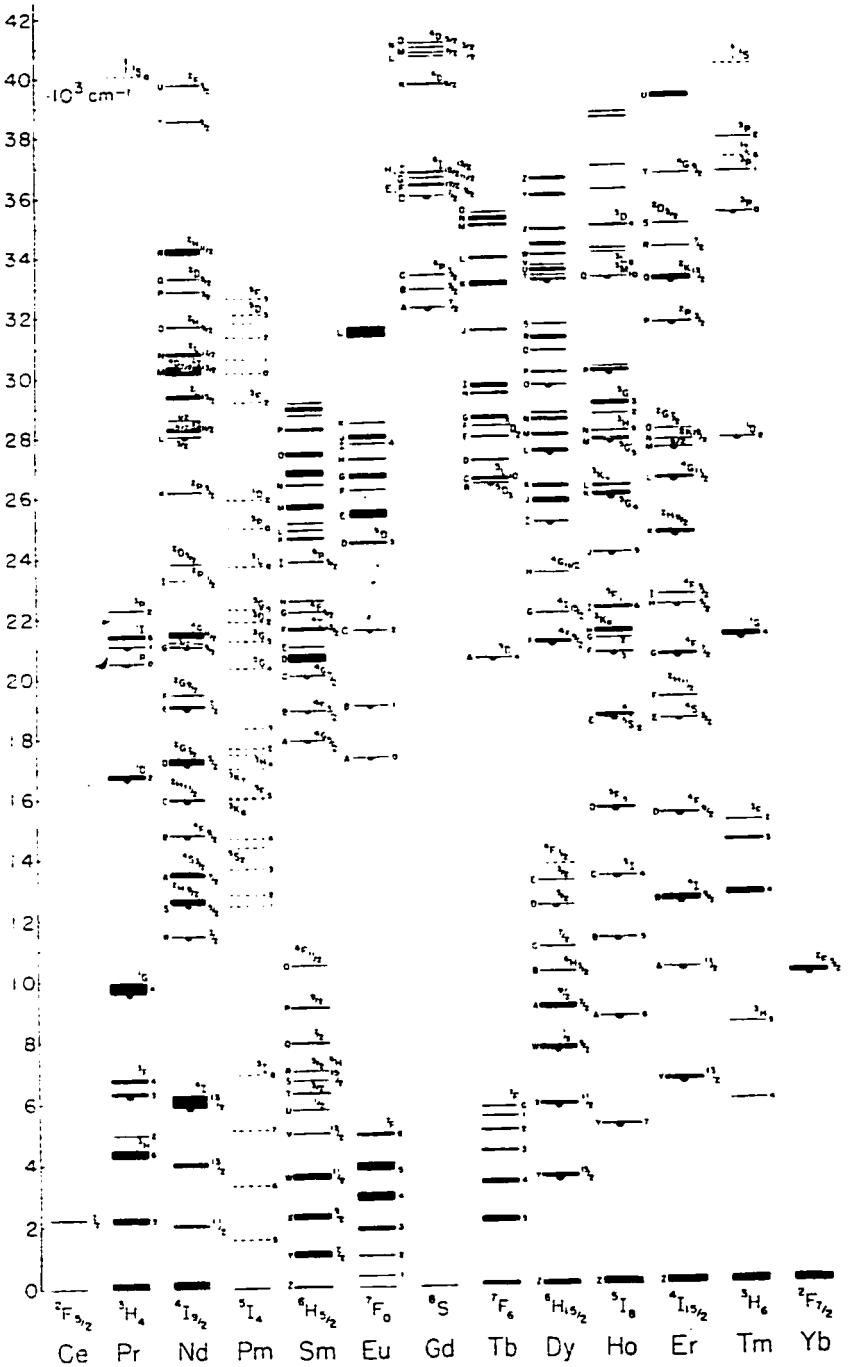

Figure 1.1.1: Observed energy levels of the rare earth ions

1.2 Eu^{3+}:Y_2O_3 NANOCRYSTALS

Much of the current research in material physics and chemistry is focused on rare earth doped nanometer-sized crystals, which are polycrystalline materials with particle diameters of less than 100nm [13]. The interest in doped nanocrystals is fueled by their potential as efficient display phosphors in opto-electronic applications since they possess enhanced optical properties [14]. The major advantage of nanocrystals over conventional bulk phosphors is their low volume to area ratio resulting in a greater fraction of atoms at the crystal surface. This advantage yields a high quantum efficiency, which in turn makes them ideal model systems for surface effect studies [14]. Nanocrystals are often described as "artificial atoms" because they approach the characteristics of atomic spectra. The optical properties of such ions tend to vary as a function of the particle size [15]. Ultimately, an in-depth understanding of enhanced properties and surface effects of doped nanocrystal phosphors will eventually lead to materials with tailored functions [14].

The search for new phosphors has led to the preparation of various forms of lanthanide-doped oxides such as: Eu^{3+} doped Y_2O_3 which exhibits a narrow emission line in the red at ~611nm [16]. Wickersheim and Lefever [17] were the first to report this red emission as part of their work at the GTE laboratories in 1964. During the same period researches at Philips were busy creating high efficiency lights by combining the narrow emission from three rare earth activated phosphors, of which Eu^{3+} was one. This new type of ultra efficient lighting would emit in the spectral regions with maximum

sensitivity towards the human color receptors. This global interest in rare earth doped systems set many researchers at the time on a quest to create the most efficient phosphor/host combination for high efficiency optical applications. Two of these researchers were Forest and Ban [18], who reported the crystal structure and luminescence properties of such red phosphors in 1969. Their work was the driving force behind the use of Eu^{3+}:Y_2O_3 as a common phosphor in optical display and lighting applications [19].

As a consequence of their work, it is now known, that cubic phase Y_2O_3 forms at high temperature and belongs to the space group Ia3. Eu^{3+} substitutes for the Y^{3+} ions, which possess C_2 and C_{3i} symmetry, where the C_{3i} sites contain an inversion center [20]. Previous studies have shown that the Eu^{3+} ions have an equal probability of randomly substituting in C_2 and C_{3i} sites (C_2/C_{3i} =1/3) [21]. The C_2 ad C_{3i} sites found in Y_2O_3 are shown in Figure 1.2.1 [22].

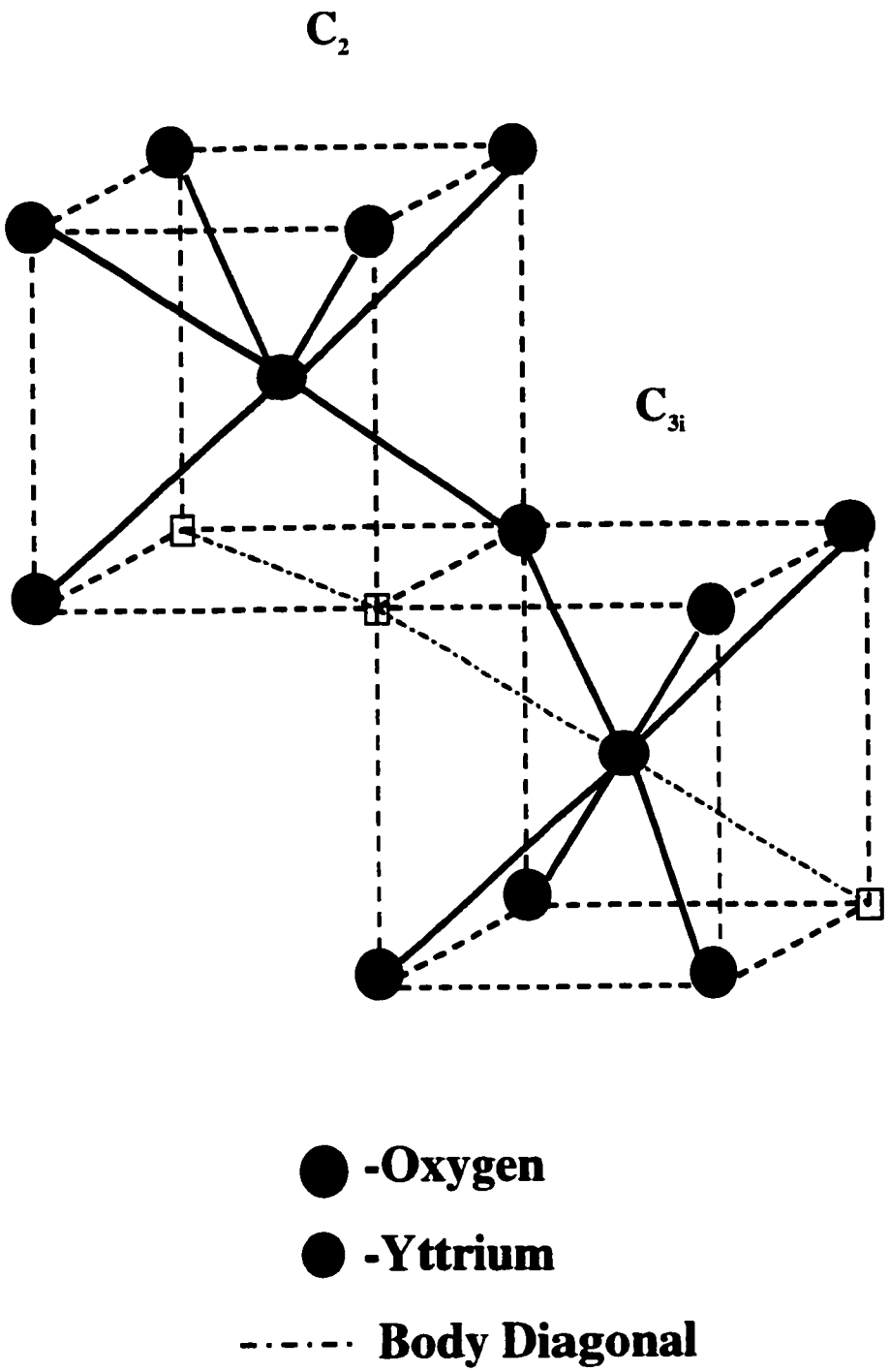

Figure 1.2.1: Pictorial Representation of the two Lanthanide (Y^{3+}/Eu^{3+}) Sites in Y_2O_3

1.3 ENERGY TRANSFER

Energy transfer is an extremely important process in solids state crystal systems because it provides an enhancement of luminescence emission resulting in a reduction of the laser threshold [23]. The general purpose of most energy transfer studies such as in this thesis is to investigate the possibility of increasing the efficiency of the phosphor. In general, the system of interest has two different types of optically active components. The introduction of an ion called the "sensitizer" or "donor" into the laser host material in addition to the ion, called the "activator" or "acceptor", responsible for laser emission. The transfer of energy from a donor ion to an acceptor ion is generally the second step in a series of three steps that normally occur in luminescent systems.

Förster [24] carried out the seminal work on resonant energy transfer in 1948. He formulated the energy transfer rate for electric dipole-dipole allowed transitions between organic molecules. Förster showed that the efficiency of energy transfer, "Z" between a donor and an acceptor, separated by a distance R, varies by a factor of $1/R^6$. One may calculate the extent of energy transfer using equation 1.3.1.

$$Z = 1/R^6 = [8.78 \times 10^{-25}\ \kappa^2 J Q n^{-4} (F_o/F - 1)] \qquad 1.3.1$$

where,

$$R = [1/Z]^{1/6}\ \text{cm} \qquad 1.3.2$$

and F_o/F is the experimentally determined ratio of fluorescence intensity in the absence of an acceptor to its value in its presence, Q is the quantum yield of the donor in the absence

of the acceptor, n is the refractive index of the medium, κ^2 is the orientation factor and J is the overlap integral which measures of the extent of overlap between the emission of the donor and the absorption of the acceptor shown as the shaded region in Figure 1.3.1.

A few years later in 1952, Dexter [25] generalized Förster's [24] theory to include transfer by means of forbidden transitions. This revised theory has since been applied to the energy transfer between dopant ions in inorganic solids. In resonant energy transfer, an excited donor ion decays to the ground state by transferring its energy to an unexcited acceptor ion without creation or destruction of photons or phonons. Dexter and Förster's combined work produced the "two-atom model", which can be used to study such systems since the transfer occurs between one donor ion and one acceptor ion. Later, Innokuti and Hirayama [26] developed the theory for the exchange coupling, which formally incorporated all variables involved in energy transfer mechanisms. Phonon-assisted energy transfer plays a major role in the infrared to visible conversion process in some phosphors which are activated with trivalent rare earth ions as shown by Hewes et al. [27], and Johnson et al. [28]. Phonon-assisted energy transfer implies a nonresonant energy transfer process where the mismatch of energy between the donor and acceptor ions is compensated through simultaneous emission and absorption of one or more phonons depending on the cutoff phonon energy of the host material.

Aside from host material influences, temperature is also an extremely important factor in energy transfer processes. Ultimately, temperature may be the key to the fully understanding energy transfer mechanisms.

Therefore, in order to optimize the performance of a phosphor, it is necessary to know in detail *(i)* what energy transfer steps are involved *(ii)* their rates, *(iii)* temperature dependence of the process and (iv) the effect of concentration of the different ions.

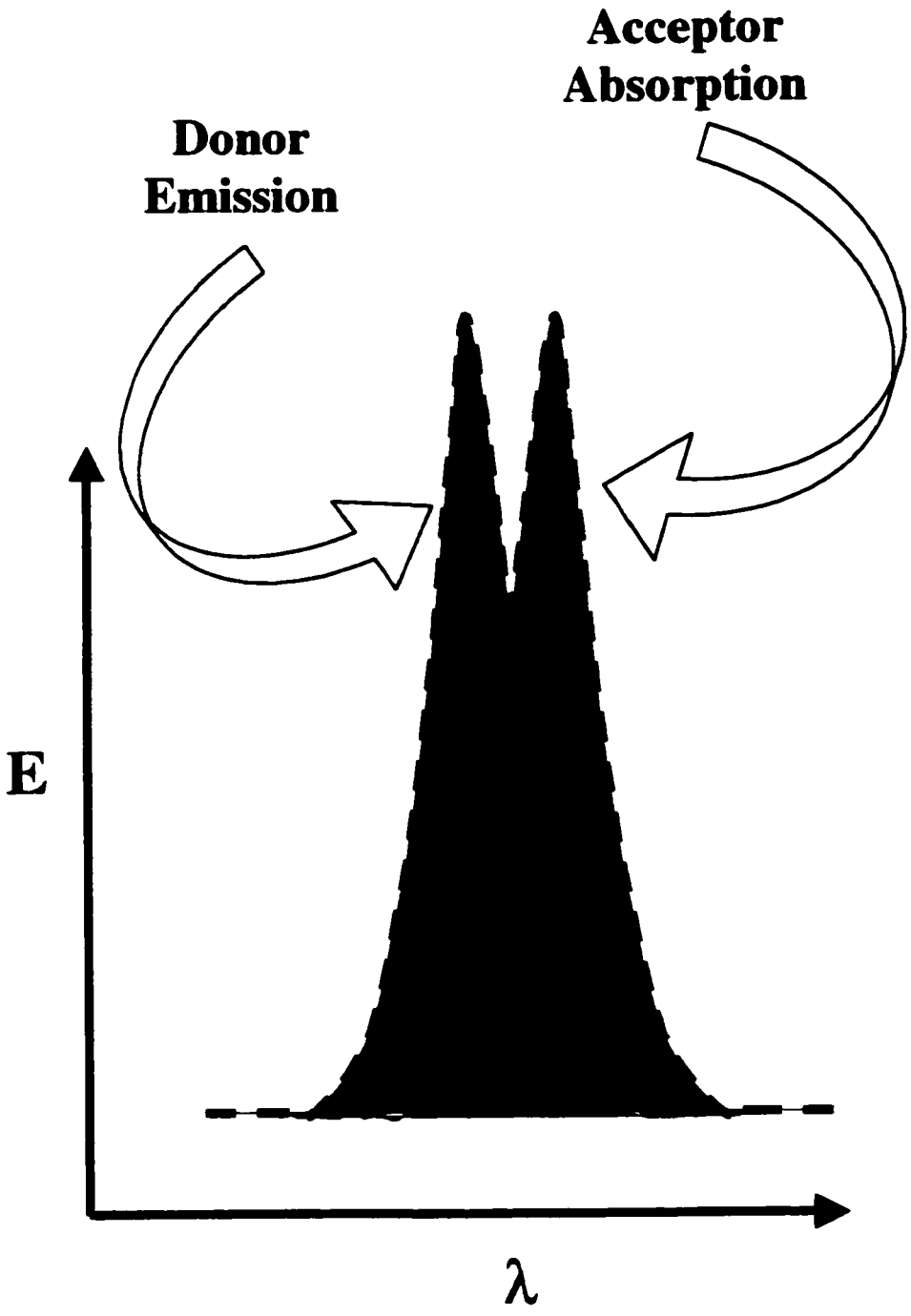

Figure 1.3.1: Schematic Representation of a Donor-Acceptor Pair Spectral Overlap Required for the Radiationless Energy Transfer as Described by Förster

1.4 STATEMENT OF THE PROBLEM

To the best of our knowledge, recent energy transfer studies of Eu^{3+}:Y_2O_3 nanocrystals have yet to relate the sample preparation method to the extent of energy transfer between Eu^{3+} ions in the two distinct sites. A better understanding of the advantages and disadvantages of the preparation method in relation to luminescence of these samples would allow for the production of more efficient Eu^{3+}:Y_2O_3 nanocrystals in the future. Thus, the aim of this study is to obtain the energy level diagram for the lowest manifolds of the ^5D and ^7F terms in Eu^{3+} doped Y_2O_3 nanocrystals by obtaining emission data and by establishing the emission transitions associated to the Eu^{3+} (C_{3i}) ions and the transitions associated to the Eu^{3+} (C_2) ions. The success of this study is possible once the following questions are addressed: *(i)* do Eu^{3+} ions have preferential occupation of C_2 versus C_{3i} sites based on site selective work, *(ii)* does temperature have an effect on the energy transfer process from $Eu^{3+}(C_{3i})$ to $Eu^{3+}(C_2)$ by observing emission in the temperature range between 298K and 77K, *(iii)* is the relative lifetime of the $^7F_2$ transition for Eu^{3+} affected by selective excitation into the different sites, *(iv)* do the optical properties, lifetimes, and site selectivity differ between Eu^{3+} doped Y_2O_3 nanocrystals and bulk samples.

CHAPTER 2

2. THEORY

The purpose of this section is to provide an overview of the theory used to understand Eu^{3+} doped crystal systems and their optical properties within a Y_2O_3 host.

2.1 SIZE EFFETCS OF NANOCRYSTAL PARTICLES

The intrigue behind nanocrystals is their distinct set of physical and chemical properties, since these properties vary systematically as a function of their particle size. This section of the thesis will introduce the chemical and physical properties intrinsic to nanocrystals as a result of their small particle diameters.

2.1.1 DENSITY OF STATES

In contrast to crystalline structures, the electronic energy levels of isolated atoms are viewed as discrete and well separated. The bands of solids are centered near the atomic energy levels of the constituent atoms. In contrast, macroscopic particles exhibit continuous energy levels since the level spacing between states is always smaller than the thermal energy at ambient temperature [14]. In nanocrystals, the density of the electronic energy levels lies between the atomic and bulk limits. In smaller diameter nanocrystals,

the threshold energy for absorption is shifted to higher energies causing the spectra to develop discrete features. This behavior is analogous to the quantum mechanical approach for a particle in a box. Recall that the spacing of the energy levels varies inversely to the square of the box size. As a result, nanocrystals can be treated as quantum particles since their discrete energy levels are an effect of their small diameters. Individual nanocrystals emit and absorb light at very discrete energies depending on their size. Figure 2.1.1.1 illustrates the discrete energy level spacing associated with nanocrystal particles [15].

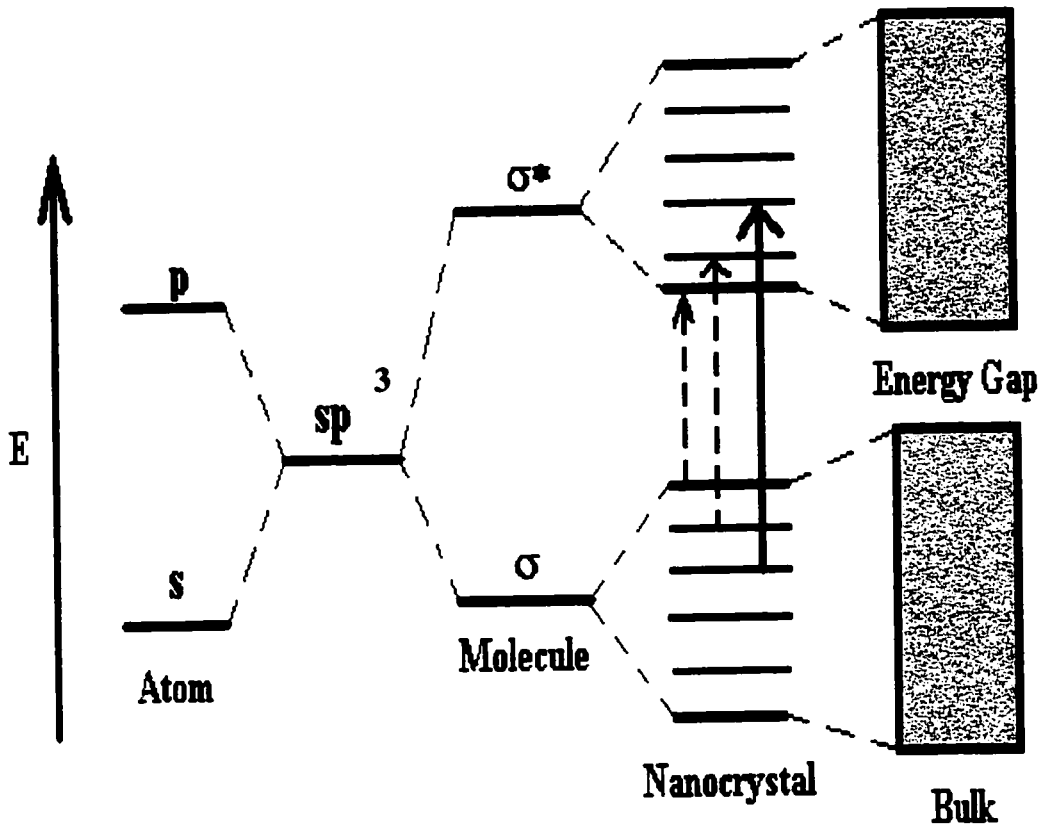

Figure 2.1.1.1: Effect of Size Evolution on the Density of Electronic States in Nanocrystals

2.1.2 THERMODYNAMIC AND PHASE TRANSITIONS

Phase diagrams have been widely used to characterize bulk materials in terms of thermodynamic variables including pressure, volume, magnetic field, and magnetization [16]. Nanometer size crystals possess distinct changes in the thermodynamics and the kinetics of their phase transitions. There is speculation that phases that are unstable or unobserved in extended solids may be prepared as nanocrystals [29].

2.1.2.2 THERMODYNAMICS: MELTING POINTS

Experiments have revealed that nanocrystal particles melt at much lower temperatures than their bulk counterpart [30]. This observation can be accounted for in the following two ways. First, the cohesive energy of a crystal is much lower than an amorphous solid since it is defined as the sum of all adjacent interactions between atoms. In small crystals, the number of atoms at the surface is large causing its cohesive interaction within the crystal matrix to be low. Second, according to thermodynamics, melting takes place at a temperature where the chemical potential of the solid and liquid are equal. Recall that the surface energy of liquids is less than solids, since liquids can assume lower surface area conformations. Thus, similar to liquids, nanocrystals possess low melting points due to their large surface area to volume ratio resulting from their small internal diameters.

2.2 SITE SYMMETRY AND OPTICAL PROPERTIES OF Y_2O_3

Site selective excitation and fluorescence spectroscopy of Eu^{3+}:Y_2O_3 has been extensively studied in recent years [16,19]. The interest in this oxide stems from its superior quality as a host lattice for spectroscopic studies [31]. R^{3+}:Y_2O_3 systems can exist in monoclinic and cubic C (bixbyite) phases with a C2/m and Ia3 space group respectively [32]. The elementary unit cell for the cubic phase contains three C_2 cation sites and a single C_{3i} cation site [32]. The cell contains 16 formula units with 32 R^{3+} cations distributed among the 24 C_2 sites and 8 R^{3+} cations distributed among the remaining 8 C_{3i} sites. Electric dipole transitions are forbidden for the C_{3i} sites, however, their spectroscopic contribution can be observed via vibronic or allowed magnetic dipole transitions [32].

Three basic physical processes determine intrinsic optical properties of a material: free carriers, lattice vibrations, and electronic transitions [13]. Insulators such as Y_2O_3, require the characterization of lattice vibrations to fully understand their optical properties. The physical and optical properties of Y_2O_3 are summarized in Table 2.2.1.

Table 2.2.1: Physical and Optical Properties for a Typical Insulator (Y_2O_3)

Material	Crystal structure	Space group	Unit cell lattice parameters (Å)	Formula per unit cell, Z	*m.p. (K)	**Transparent Optical Region μm
Yttrium Oxide (Y_2O_3)	Cubic (bixbyite) monoclinic	Ia3 C2/m	10.603	16	T_p = 2640 T_m = 2710	2.9-7.1

*T_p: phase change temperature; T_m: melting temperature
**Region with absorption coefficient <1cm^{-1}

Thus, site selective emission and fluorescence lifetime studies of Eu^{3+}:Y_2O_3, would be the most effective tools in identifying its distinct sites and their different photon transfer mechanisms respectively.

2.3 ELECTRONIC ENERGY LEVELS OF Eu (III) ION

As previously stated, lanthanide elements possess a unique electronic structure. The optically active 4*f* electrons are strongly shielded by the outer $5s^25p^6$ electron shells. The large orbital radii for these electrons provide excellent shielding for the 4*f* electrons. Thus, causing lanthanide spectra to exhibit similar characteristics to atomic spectra. Therefore, the crystal field splitting is directly determined by the local site symmetry of the rare earth ion. Knowledge of the point symmetry enables one to determine the

selection rules that govern the optical transitions between different crystal field levels [33].

It can be assumed that nuclear interactions and the shielding effects cause each of the $4f$ electrons to move spherically symmetric in an electrostatic field [34]. This assumption is known as the central field approximation, where the eigenstates of the $4f$ electrons are calculated by assuming their interaction is negligible. The Hamiltonian that describes the energies of the free ion states is found to be a combination of four fundamental terms such that it may be described by the sum of their individual Hamiltonians expressed in the following equation:

$$H_{FI} = H_o + H_c + H_r + H_{so} \qquad 2.3.1$$

The first term defines the kinetic energy for all $4f$ electrons and is given by:

$$H_o = -\hbar^2 / 2m \sum_{i=1}^{N} \nabla_i^2 \qquad 2.3.2$$

Where ∇^2_i, is the Laplacian operator which is equal to the following partial derivative: $\partial/\partial x + \partial/\partial y + \partial/\partial z$. Since H_o is spherically symmetric its only effect is an overall energy shift of all $4f^n$-levels but it does not remove the degeneracy. For spectroscopic purposes it is therefore neglected.

The second term in the Hamiltonian describes the Coulombic attraction between the nucleus and $4f^n$ electrons, which partially removes the degeneracy. This term known as H_c is given by:

$$H_c = \sum_{i=1}^{N} Z_{eff} \times e^2 / r_i \qquad 2.3.3$$

Z_{eff}, the effective nuclear charge, is determined by the nature of the outer electronic sub-shells and r_i, is the inter-atomic distance between the electron and the nucleus.

The third term of the Hamiltonian operator (H_r), describes the electrostatic repulsion between two electrons with charges denoted $Z_A e$ and $Z_B e$ respectively. Equation 2.3.4 represents the electrostatic repulsion contribution to the Hamiltonian, where r_{ij}, is the inter-electron distance.

$$H_r = \sum_{i<j}^{N} e^2 / r_{ij} \qquad 2.3.4$$

The spin-orbit interaction is the final contribution to the Hamiltonian. H_{so}, represents the magnetic interactions for which ι_i and s_i are the nuclear spin quantum number and spin quantum number respectively. The overall contribution to H_{so} is given by equation 2.3.5.

$$H_{so} = \sum_{i=1}^{N} \xi(r_i) S_i \times \ell_i \qquad 2.3.5$$

where,

$$\xi(r_i) = \frac{\hbar}{2m^2c^2r_i} + \frac{dU(r_i)}{dr_i} \qquad 2.3.6$$

and $U(r_i)$, is the potential energy required to displace an electron. In essence, it is equation's 2.3.3 and 2.3.4 that determine the energy level structure for the 4*f* electrons. Electrostatic repulsions cause the splitting of the Russell Saunders ^{2S+1}L terms, referred to as the grouping of microstates of equivalent energy. It is the spin orbit coupling term that further splits the ^{2S+1}L terms into $^{2S+1}L_j$ energy level terms, where the degeneracy is equal to 2J+1[33].

Thus, the general Hamiltonian that determines the electronic energy levels of the $4f^n$ electrons is as follows, where N, is the number of 4*f* electrons for a given ion system.

$$H = -\hbar^2/2m \sum_{i=1}^{N} \nabla_i 2 - \sum_{i=1}^{N} Z_{eff} \times e^2 / r_i + \sum_{i<j}^{N} e^2 / r_{ij} + \sum_{i=1}^{N} \xi(r_i) S_i \ell_i \qquad 2.3.7$$

In atomic theory, the relative influences of H_{RE} and H_{SO} are limited when either $H_c >> H_{SO}$ or when $H_{SO} >> H_c$. When $H_c >> H_{SO}$, the spin-orbit interaction produces only a small perturbation to the overall energy structure, resulting in the Russell-Saunders coupling scheme. When $H_{SO} >> H_c$, the electrostatic interaction has a minimal effect, ensuing the j-j coupling scheme. Thus, the calculations for the electronic energy levels of

rare earth ions is much more complex due to the fact that $H_{RE} \cong H_{SO}$. This situation is termed *intermediate coupling* [34].

As of yet, only the free ion has been considered. In reality the ion will never be totally isolated but experience an anisotropic electrostatic field produced by the surrounding atoms known as the crystal field. Therefore, the complete Hamiltonian including both the free ion and crystal field components is expressed as follows:

$$T_{otal} = H_{FI} + H_{CF} \qquad 2.3.8$$

The crystal field leads to further splitting of the 2J+1 fold degenerate free ion states into Stark levels (crystal field levels) [33]. It is therefore necessary to distinguish between two groups of ions, the ions with an odd number of $4f$ electrons, which are called *Kramers ions*, and those with an even number, which are called *non-Kramers ions*. If the crystals field is of low symmetry, as is the case in a glass, the free ion levels of Kramers ions are split into (J+1/2) and those of non-Kramers ions into (2J+1) Stark levels [34].

The Eu^{3+} ion possesses an electronic configuration of $4f^6$, where its ground state energy level is ^7F_o [33]. Therefore, each energy level can be split into 2J+1 sub-level structures, which are sensitive to the local crystal field surrounding the Eu^{3+} ion since it is a non-Kramers ion [33].

Thus the electronic splitting of energy states within the overall energy level diagram for Eu^{3+} is given in Figure 2.3.1.

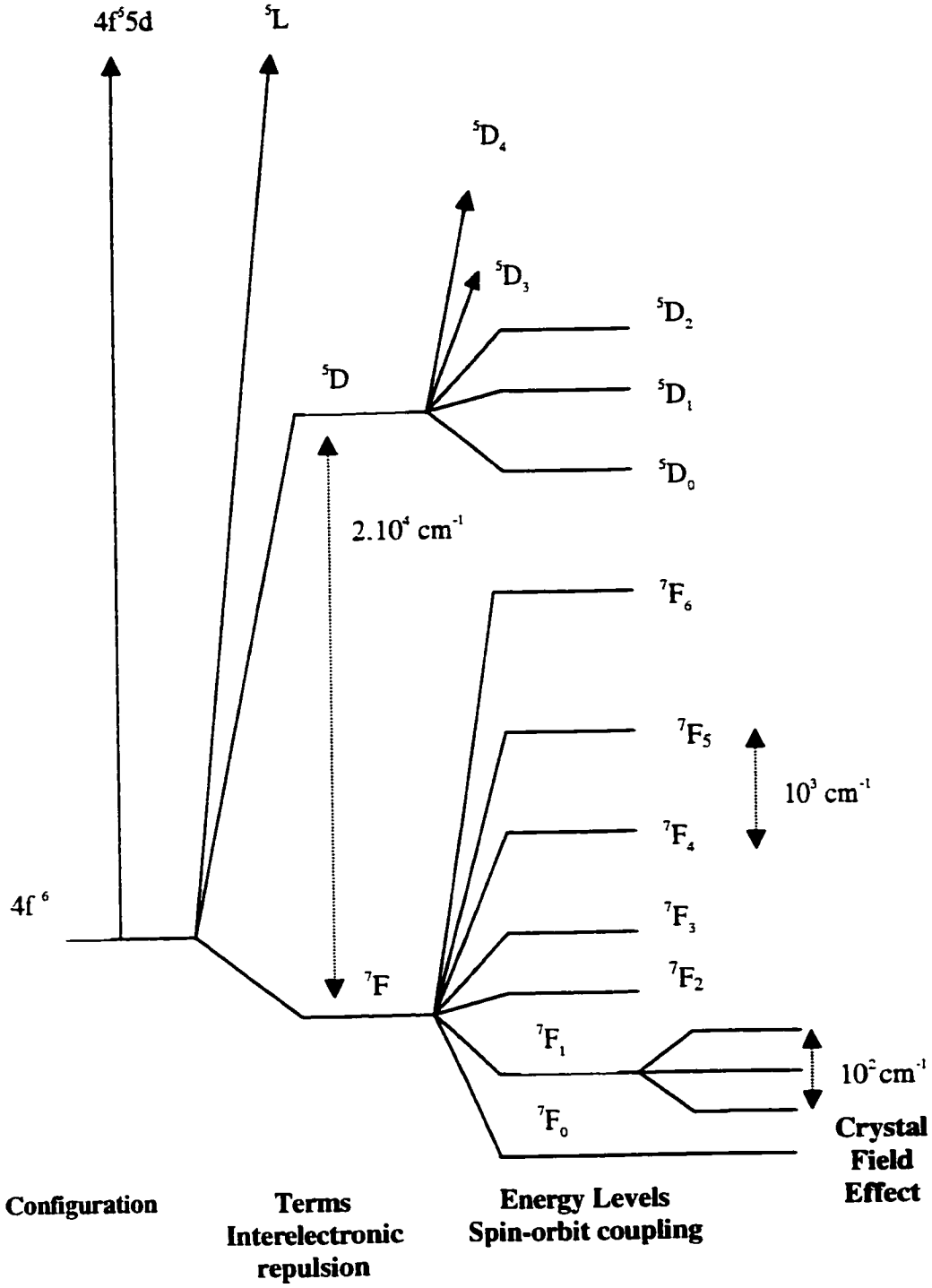

Figure 2.3.1: Energy level diagram and splitting of Eu^{3+}

2.4 SELECTION RULES FOR Eu (III)

Selection rules determine whether a transition is forbidden or allowed. Classically, a molecule possessing a *temporary* oscillating dipole of frequency υ, will interact with the electromagnetic field and absorb or emit a photon at the same frequency. For emission and absorption spectra, this temporary dipole is expressed in terms of the transition dipole moment; μ [35].

In lanthanide doped systems, radiative processes are a result of the interactions between the 4*f* electronic shell and the external electromagnetic field [36]. The matrix element in equation 2.4.1 will determine the extent of a radiative transition between states *a* and *b*.

$$\langle a | \vec{\mu} \bullet \hat{\varepsilon} | b \rangle \qquad 2.4.1$$

where $\vec{\mu} \bullet \hat{\varepsilon}$, is the appropriate dipole operator. For electric dipole interactions the operator is odd given by $\vec{\mu}_e \bullet \hat{\varepsilon}_E$, where $\vec{\mu}_e = \Sigma\, e\, \vec{r}_i$ and $\hat{\varepsilon}_E$ is the unit polarization vector parallel to the field E, of the electromagnetic radiation.

For electric dipole transitions involving 4*f* electrons, the following selection rules apply:

$$\Delta l = \pm 1 \qquad 2.4.2$$

$$\Delta S = 0$$

$$|\Delta L| \leq 6$$

$|\Delta J| \leq 6$ unless J or J' = 0, then $|\Delta J| = 2,4,6$

where $\Delta l = \pm 1$, known as Laporte's rule, states that the parity of the final state must be different from the parity of the initial state (i.e. $+ \leftrightarrow -$).

For magnetic dipole interactions, the dipole operator is an even operator given by $\vec{\mu}_m \bullet \hat{\varepsilon}_B$ where $\vec{\mu}_m$ is represented as in equation 2.4.3 and $\hat{\varepsilon}_B$ is the polarization vector perpendicular to the field B of the electromagnetic radiation:

$$\vec{\mu}_m = \sum_i \frac{-\hbar}{2mc}(l_i + g_e s_i) \qquad 2.4.3$$

where l is the angular momentum quantum number, and s is the spin quantum number.

Thus, the selection rules for the magnetic dipole interactions are given by:

$$\Delta l = 0 \qquad 2.4.4$$

$$\Delta S = 0$$

$$\Delta L = 0$$

$$\Delta J = 0, \pm 1 \text{ (not } 0 \leftrightarrow 0)$$

$$\Delta M_J = 0 \ (\sigma \text{ polarization})$$

$$\Delta M_J = \pm 1 \ (\sigma \text{ and } \pi \text{ polarization})$$

The intensity of a transition depends on the probability of such a transition occurring. Therefore, a transition that has a high probability of occurring will produce an intense emission or absorption peak. Equally, if a transition is forbidden according to the selections rules, then that transition will produce low intensity emission or absorption lines since there is a low probability that the transition will occur [35]. The probability of a transition occurring between states *a* and *b* is expressed in equation 2.4.5.

$$P_{ab} = [\langle a | \bar{\mu} \bullet \hat{\varepsilon} | b \rangle]^2 = 1 \qquad 2.4.5$$

As previously mentioned for in case of rare-earth ions, the selection rules are primarily determined by site symmetry, however, due to the weak crystal field, the selection rules of the free ion are still relevant. Electric dipole transitions within a f^n configuration are allowed due to environmental perturbation. For point groups of very low symmetry such as C_2, C_s or C_1, all $f \leftrightarrow f$ transitions are allowed, therefore the only consideration is the relative magnitude of the contribution from each of the dipole processes. Table 2.4.1 summarizes the transitions allowed for Eu^{3+} ions in C_2 and C_{3i} site symmetry environments as determined by the selection rules.

Table 2.4.1 Allowed Emission Transitions According to Selection Rules for: Eu^{3+} ions in C_2 and C_{3i} Site Symmetry Environments

SITE SYMMETRY	TRANSITION	ALLOWDNESS
C_2	$^5D_0 \rightarrow {}^7F_0$	Forbidden
	$^5D_0 \rightarrow {}^7F_1$	Magnetic Dipole
	$^5D_0 \rightarrow {}^7F_2$	Electric Dipole
	$^5D_0 \rightarrow {}^7F_3$	Forbidden
	$^5D_0 \rightarrow {}^7F_4$	Electric Dipole
C_{3i}	$^5D_0 \rightarrow {}^7F_0$	Forbidden
	$^5D_0 \rightarrow {}^7F_1$	Magnetic Dipole

2.5 ENERGY TRANSFER THEORY

The general purpose of energy transfer studies is to investigate the possibility of increasing the efficiency of the phosphor or laser [21]. The energy levels of rare earth ions are not strongly affected by the host material. However, the nature of the host material is important to the energy transfer process for several reasons. In many cases the energy transfer process needs the assistance of phonons, whose frequency and population at a specific temperature depend on the nature of the material [37]. Thus, a host with a low phonon energy cut off is ideal in energy transfer studies since the probability of bridging the energy gap between two levels is high. However, one should be aware that

complications could arise due to the influence of the thermal vibrations on the kinetics of the excitation and de-excitation (decay) of the relevant levels of the sensitizer and activator. In essence, thermal vibrations may effect the positions and line widths of transitions. Although such effects may be small, they can become serious in the case of resonant transfer [37].

A radiative transition is whereby the "donor" may relax to a lower energy state by emitting a photon. The photon emitted may then be absorbed by the acceptor ion. The probability of this process occurring depends on the absorption coefficient and the total number of acceptor ions present. However, the photon emitted may also be absorbed by another "donor" ion in close proximity (i.e.<10Å) [37]. Thus, the absorption of energy in this case depends on the spectral overlap between the absorption and the emission bands of the "donor" and the number of donor ions in the crystal.

In the absence of photon emission, another donor ion may be excited to a higher energy level. This process is known as "migration of energy". This process depends on both the concentration and the spectral overlap between the absorption and the emission bands of the donor [24].

In non-radiative relaxation, the donor ion may decay to its ground state through a non-radiative transition. In this case, the energy is transferred to the phonon basin. This process provides an additional decay mechanism to the donor ion, causing the lifetime of the donor to be shorter. This arises from the Van der Waals' interaction between the two

ions involved in the energy transfer process. However, since the interactions are weak, no relevant changes in the energy levels of either donor or acceptor are observed. Thus, this allows one to categorize all energy transfer processes as either non-radiative or radiative. Figure 2.5.1 shows the five major stages involved in an energy transfer process.

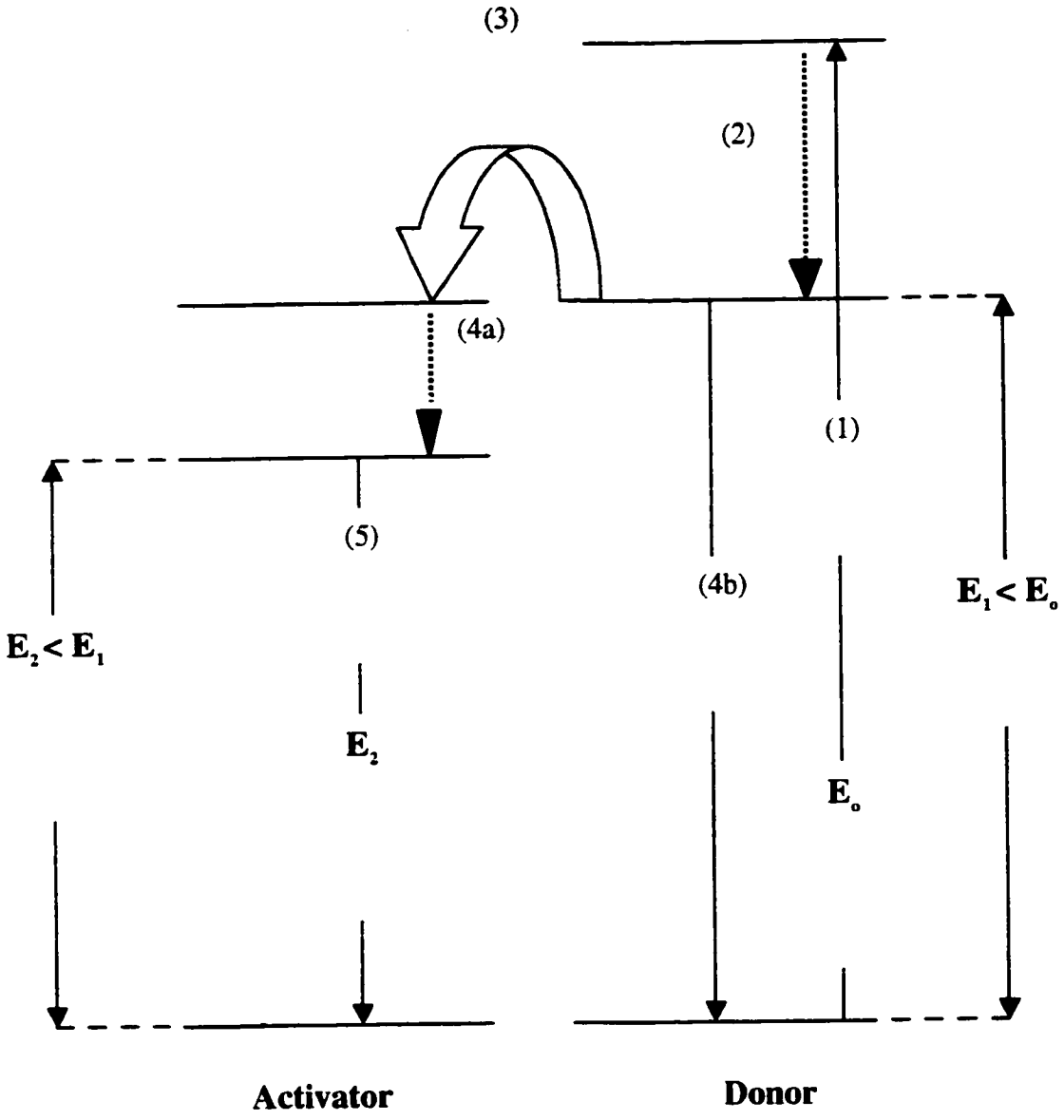

Figure 2.5.1: Schematic diagram of the five major stages involved in an energy transfer process

Where (1) is the absorption of a photon of energy ~E_o by the donor, (2) is the relaxation of the lattice surrounding the donor by an amount such that the available electronic energy in a radiative transition from the donor is $E_1<E_o$ (3) Transfer of energy E_1 to the activator, (4a) is the relaxation around the activator such that the available electronic energy in a radiative transition is $E_2<E_1$. (4b) is the relaxation around the donor to a state similar (but not necessarily identical) to its original unexcited state, and (5) is the emission of energy E_2.

CHAPTER 3

3. EXPERIMENTAL

3.1 CRYSTAL GROWTH

Nanosized Y_2O_3 crystals doped with 1, 5 and 10mol % Eu_2O_3 ($Y_{1.98}Eu_{0.02}O_3$ $Y_{1.9}Eu_{0.1}O_3$and $Y_{1.8}Eu_{0.2}O_3$ respectively) were prepared using a combustion synthesis procedure [38, 39]. Details of the synthesis have been given in a previous article [40]. The synthesis reaction is:

$$\mathbf{6M(NO_3)_3 + 10NH_2CH_2COOH + 18O_2 \rightarrow 3M_2O_3 + 5N_2 + 18NO_2 + 20CO_2 + 25H_2O}$$

where M=Y, Eu. A glycine-to-metal nitrate molar ratio of 1:2:1 was employed to prepare the precursor solution. According to literature, this nitrate rich composition should allow the formation of small size yttria particles. It has been reported that particle sizes of 8 and 40 nm were obtained in the case of $Y_{1.80}Eu_{0.20}O_3$ materials [39] for glycine-to-metal nitrate molar ratio of 1:0:1 and 1:3:1, respectively. After the combustion, the powders were fired for 1 hour at 500 °C in order to decompose the residual nitrate ions.

In addition nanosized Y_2O_3 crystals doped with 1, 5 and 10mol % Eu_2O_3 ($Y_{1.98}Eu_{0.02}O_3$ $Y_{1.9}Eu_{0.1}O_3$and $Y_{1.8}Eu_{0.2}O_3$ respectively) were prepared using the hydrolysis synthesis. This procedure consists of the reaction between two solutions (i.e. Solution A and Solution B) prepared separately after which solution A is added drop wise

to solution B with the use of a burette at a controlled rate (10 drops per minute) while stirring vigorously. Solution A was prepared by dissolving ~16g of $Y(NO_3)_3 \cdot 5H_2O$ and ~0.16g of $Eu(NO_3)_3 \cdot 5H_2O$ in ~50ml of spectrograde ethanol for the 1mol% doped sample. The resulting solution was then stirred for 2hours at room temperature. Solution B was prepared by mixing 10% wt of the surface modifier Tween-80® and Emulsogen-OG with respect to Eu_2O_3/Y_2O_3 in 50 ml of aqueous ammonium hydroxide (pH>10). The resulting solution was then stirred for one hour at room temperature.

The gel obtained following the addition of Solution A to solution B was separated in a centrifuge at a rate of 6000 rpm for 30 min. The aqueous solution was removed by refluxing in toluene using a water trap. The toluene was then evaporated yielding a powder, which was further dried in an oven at 60°C for 24 hours. The final product was isolated as a fine white powder after heat treatment in a box furnace at 450°C for 2 hours in ambient atmosphere.

For comparative purposes, 1, 5 and 10 mol % bulk samples ($Y_{1.98}Eu_{0.02}O_3$ $Y_{1.9}Eu_{0.1}O_3$and $Y_{1.8}Eu_{0.2}O_3$ respectively) were prepared by intimately mixing Y_2O_3 (Aldrich, 99.99 %) and Eu_2O_3 (Aldrich, 99.99+ %), pressing the powders into pellets under 10 tons of pressure and firing them in air at 1500 °C for 24 hours. At this temperature, the optimum homogeneity (verified using scanning electron microscopy) was obtained. Spectroscopic measurements were carried out on a sample, which had undergone this heat treatment. All yttria samples were kept in air without any further precaution.

3.2 SPECTROSCOPY

3.2.1 VISIBLE EMISSION STUDIES

Visible emission spectra excited at 488 nm and 514.5 nm were obtained using a Sabre Innova 20W argon ion laser. Site selective emission was carried out using a tunable dye laser, (Spectra Physics 375) operating with Rhodamine 6G, (10^{-3} mol/dm^3 in ethylene glycol) and pumped by the Sabre Innova. All spectra were recorded using a Jarrell-Ash 1-meter Czerny Turner double monochromator with a maximum slit width of 200 μm. The gratings are mounted on a cosecant bar driven by a stepper motor with a step size of 0.01 cm^{-1}/step. The signal was monitored by an RCA-C31034-02 photomultiplier with a flat spectral response from 200–850 nm. The photomultiplier tube was water cooled in order to maintain the count rates of background noise below 10 counts/second. The photomultiplier signals were processed by a preamplifier, model SR 440 Stanford Research Systems. The preamplifier contains four wide bandwidth, dc-coupled amplifiers designed to be used independently or cascaded to provide gains of 5,25,125, and 625. This allows for the amplification of the output from the photomultiplier tube to the photon counter.

A gated photon counter, model SR400 Stanford Research Systems interfaces the data acquisition software to the spectroscopic hardware. Signals are recorded using a computer equipped with the Stanford SR465 software data acquisition/analysis system. A schematic representation of the experimental setup is given in Figure 3.2.1.1.

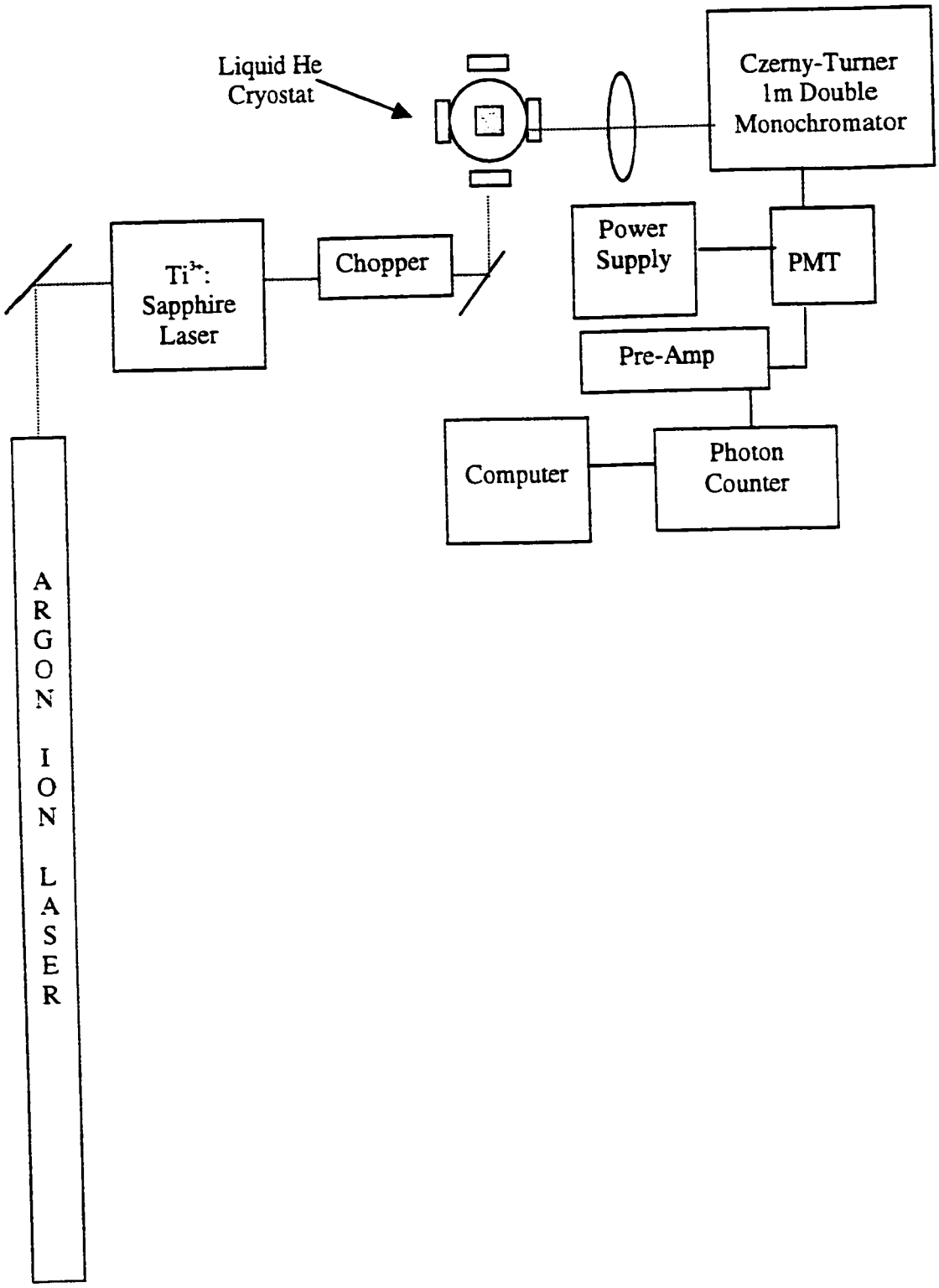

Figure 3.2.1.1: Schematic arrangement of the apparatus for the measurement of the emission spectra and decay times.

3.2.2 LIFETIME MEASUREMENTS

Fluorescence lifetimes at 580.0 nm and 582.6 nm were obtained using an Argon ion laser/Rhodamine 6G laser excitation setup. The excitation light was modulated by a chopper (SR450 Stanford Research Systems). The preamplifier processed the photomutiplier signals, which were in turn amplified to a gated photon counter (Stanford Research 400), which recorded all decay times.

3.2.3 RAMAN SCATTERING

Raman spectroscopy of the Y_2O_3 host was carried out in order to observe Raman scattering and determine the cut-off phonon energy of the lattice. A Coherent Sabre Innova laser was used to pump a Spectra Physics Model 3900 titanium sapphire (Ti^{3+}: Al_2O_3) laser in order to obtain the 750nm and 760nm excitation wavelengths. All Raman scattering was collected using a Jarrel-Ash 1m monochromator. Light scattered at $\pi/2$ from the incident beam was monitored with an RCA C31034-02 photomultiplier operating in the photon counting mode.

3.2.4 DIFFUSE REFLECTANCE (UV-VIS Region)

Diffuse reflectance spectra in the UV-visible region were measured using (a 0.2 mm quartz cell) a Shimadzu UV-265 spectrophotometer equipped with an integrating

sphere and the signal detected with a R-466U photomultilier tube. The standard white reflecting plate contained $BaSO_4$ (Eastman Kodak White reference standard).

3.2.5 DIFFUSE REFLECTANCE (FTIR)

The diffuse reflectance spectrum in the IR region was measured using a Nicolet Magna 760 FTIR spectrometer. The sample was mixed with KBr (about 10:1 KBr:Sample) and the spectrum was measured using pure KBr as a reference.

All spectroscopic measurements were carried out at 298K and 77K with the exception of diffuse reflectance and Raman experiments, which were carried out at room temperature only.

3.2.6 POWDER X-RAY DIFFRACTION

X-ray Powder diffraction was carried out on a Philips diffractometer equipped with a PW 1050/25 focusing goniometer, which has been automated with the VisX122D system from Diffraction Technologies. The Ni filtered K_α radiation of Cu was used ($\lambda_{K\alpha 1}$=1.54051 Å). The reflection geometry was used with the powdered samples packed in the cavity carved in the window of a plexiglass holder, which gives a broad scattering hump centered at ~12°(2θ). The diffraction patterns were recorded in the range 5 to 60°(2θ), in the step scanning mode, at an angular velocity of 1°(2θ)/min., with a step of 0.02°(2θ). The TracesV5 software from Diffraction Technologies was used for data

accumulation and processing. A Si pellet from Philips was used as the standard for linewidth and position. X-ray diffraction experiments were performed in collaboration with Dr. Georges Dénès in the Department of Chemistry & Biochemistry at Concordia University.

3.2.7 SCANNING ELECTRON MICROSCOPY (SEM)

For the SEM work, images were recorded with a Hitachi 520 microscope and S-5080 camera fitted with a Polaroid 545 film holder. Polaroid type 52 positive film was used. SEM experiments were performed in collaboration with Dr. Narinder Kapoor in the Department of Biology at Concordia University.

CHAPTER 4

4. RESULTS & DISCUSSION

4.1 EFFECT OF $Eu^{3+}(C_2)$ AND $Eu^{3+}(C_{3i})$ IONS ON EMISSION SPECTRA

For C_2 symmetry sites all $2J+1$ crystal field components of the $^5D_0 \rightarrow {}^7F_J$ transitions should be observable, but for C_{3i} lattice sites only the following transition is allowed according to the selection rules: $^5D_0 \rightarrow {}^7F_1$ [20]. Figures 4.1.1 and 4.1.2 show the room temperature and 77K luminescence spectra for the 1.0mol% Eu^{3+}:Y_2O_3 bulk sample respectively. At both temperatures, the most intense emission band was found at ~611nm, which corresponds to the hypersensitive $^5D_0 \rightarrow {}^7F_2$ transition for Eu^{3+} ions in C_2 sites [15]. From the spectral data collected, an energy level diagram for the $Eu^{3+}(C_2)$ and $Eu^{3+}(C_{3i})$ ions was constructed and shown in Figure 4.1.4, which is in excellent agreement with work on Eu^{3+}:Y_2O_3 single crystals reported by Heber et al. [20]. In addition, Figure 4.1.3 confirms that peak shape and positions were similar for the emission spectra of both Eu^{3+}:Y_2O_3 nanocrystals prepared by the hydrolysis and combustion method. However, upon closer examination of Figure 4.1.3 it was observed that both nanocrystal samples expressed a slight blue shift in the spectrum in comparison to the bulk sample of equal concentration. Previous studies [41-43], have reported the blue-shift phenomena in emission spectra of nanostructured semiconductor materials. However, few reports have been made on the phenomena of nanostructured rare earth compounds. In comparison to a semiconductor, Eu^{3+}:Y_2O_3 is a different kind of

luminescent material because of the different role it plays in luminescence [44]. However, in general, a semiconductor belongs to the group of luminescent materials with recombination luminescent centers. It is the recombination of the electron in the conduction band and the hole in the valence band that causes luminescence. Therefore, it may be possible that a larger band gap due to quantum confinement causes the blue shift phenomena observed with the 1mol% Eu^{3+}:Y_2O_3 nanocrystals.

The peaks at 580.0nm, 587.5nm, and 592.5nm are assigned to the $^5D_0 \rightarrow {}^7F_0$, $^5D_0 \rightarrow {}^7F_{1a}$, $^7F_{1b}$, and $^7F_{1c}$ respectively for the Eu^{3+} ions in the C_2 sites. Contrary to what was expected, the intensity of the C_2-type emission at 580.0nm was less intense at 298K, suggesting a reverse energy transfer process from the $^5D_0(C_2)$ level to the $^5D_0(C_{3i})$ over the energy gap of ~90cm^{-1}. The emission observed in the 592nm region becomes more complex at low temperature with the $^5D_0 \rightarrow {}^7F_1$ manifold being a superposition of both C_2 and C_{3i}-type emission, where the peak at 596nm is a vibronic transition of $Eu^{3+}(C_{3i})$ [32]. According to selection rules, the $^5D_0 \rightarrow {}^7F_3$ and $^5D_0 \rightarrow {}^7F_4$ transitions should be further split by the crystal field into 2J+1 Stark levels, where J is equal to 3 and 4 respectively. However, it is evident from Figure 4.1.2, that there exists more than the expected number of Stark levels. To the best of our knowledge, previous work has not assigned these transitions to either site, however C_2 type emission would be expected to dominate since it is both electric and magnetic dipole allowed. As expected, line-widths were directly proportional to temperature. At low temperature, line widths were narrow giving rise to sharp peaks since the non-radiative component of the transition is severely reduced at

lower temperatures. The transitions observed for the Eu^{3+}:Y_2O_3 bulk sample at 77K excited at 514.5nm are given in Table 4.1.1.

Table 4.1.1: Low Temperature Luminescence Observed Between 580-600nm for 1mol% Eu^{3+}:Y_2O_3 Bulk Sample Excited at 514.5nm

Transition/Site	Peak Position (nm)
$^5D_0 \rightarrow {}^7F_0(C_2)$	580.4
$^5D_0 \rightarrow {}^7F_{1a}(C_{3i})$	582.2
$^5D_0 \rightarrow {}^7F_{1a}(C_2)$	587.5
$^5D_0 \rightarrow {}^7F_{1b}(C_{3i})$	592.5
$^5D_0 \rightarrow {}^7F_{1b}(C_2)$	593.1
C_{3i} Vibronic Transition	596.0
$^5D_0 \rightarrow {}^7F_{1c}(C_2)$	599.6
$^5D_0 \rightarrow {}^7F_3$	645-675
$^5D_0 \rightarrow {}^7F_4$	685-715

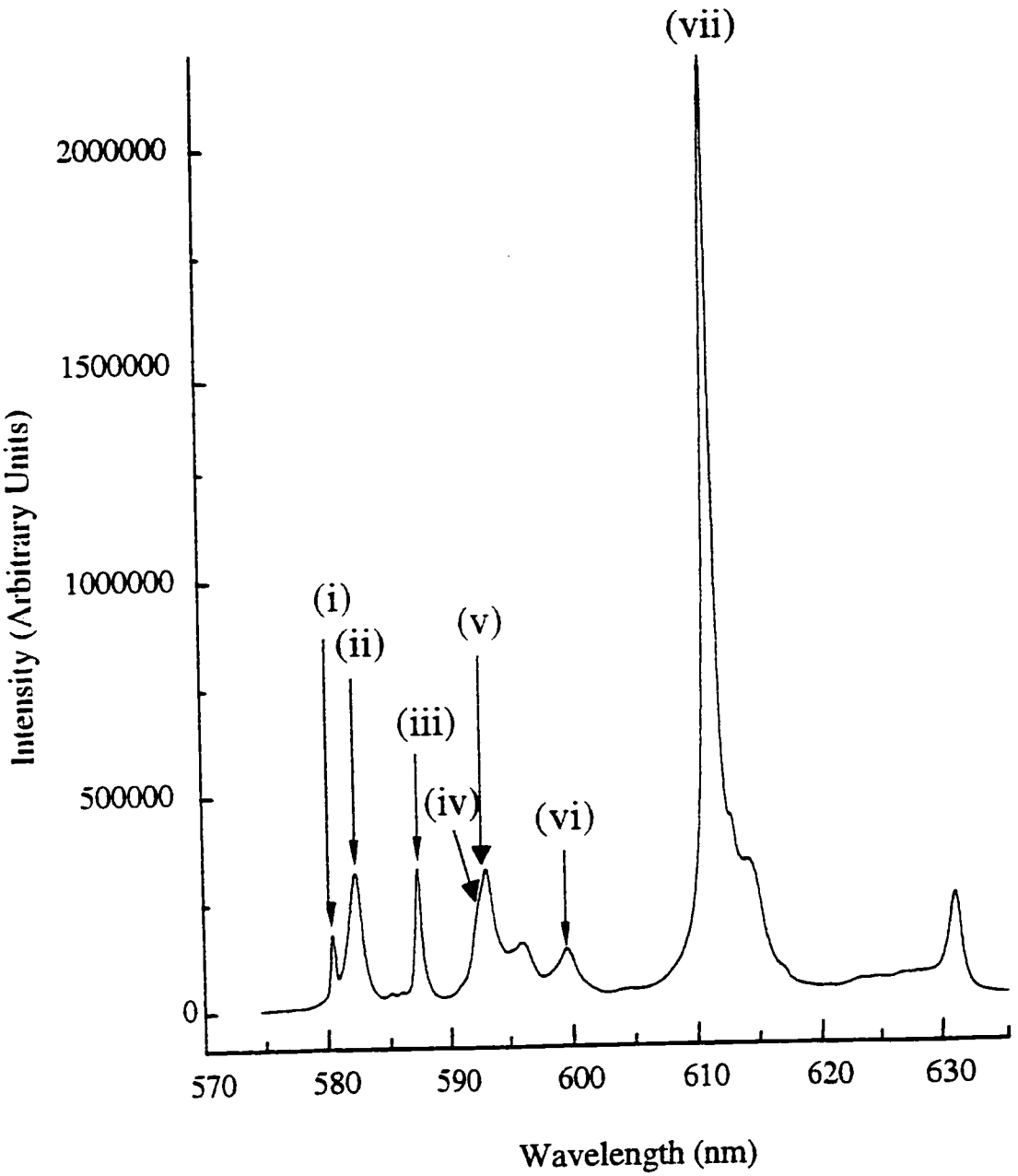

Figure 4.1.1: Room Temperature Emission Spectrum of 1mol% Eu^{3+}:Y_2O_3 Bulk sample, λ_{ex} = 514.5nm; (i) $^5D_0 \rightarrow {}^7F_0(C_2)$, (ii) $^5D_0 \rightarrow {}^7F_{1a}(C_{3i})$, (iii) $^5D_0 \rightarrow {}^7F_{1a}(C_2)$, (iv) $^5D_0 \rightarrow {}^7F_{1b}(C_{3i})$, (v) $^5D_0 \rightarrow {}^7F_{1b}(C_2)$, (vi) $^5D_0 \rightarrow {}^7F_{1c}(C_2)$, (vii) $^5D_0 \rightarrow {}^7F_2(C_2)$

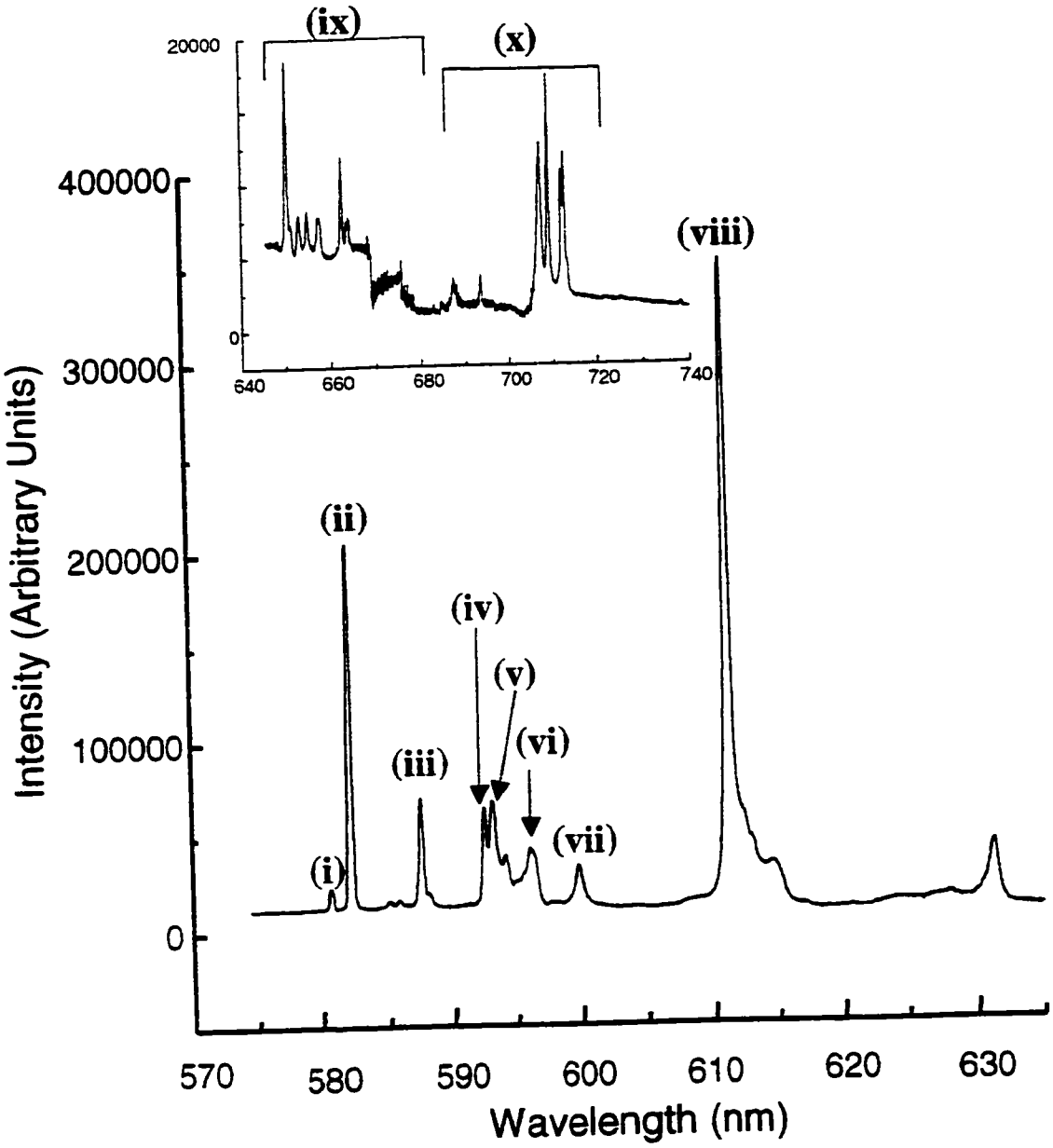

Figure 4.1.2: Low Temperature (77°K) Emission Spectrum of 1mol% Eu3+:Y_2O_3 Bulk, λ_{ex}=514.5nm; (i) $^5D_0 \rightarrow {}^7F_0(C_2)$, (ii) $^5D_0 \rightarrow {}^7F_{1a}(C_{3i})$, (iii) $^5D_0 \rightarrow {}^7F_{1a}(C_2)$, (iv) $^5D_0 \rightarrow {}^7F_{1b}(C_{3i})$, (v) $^5D_0 \rightarrow {}^7F_{1b}(C_2)$, (vi) C_{3i} Vibronic transition, (vii) $^5D_0 \rightarrow {}^7F_{1c}(C_2)$, (viii) $^5D_0 \rightarrow {}^7F_2(C_2)$, (ix) $^5D_0 \rightarrow {}^7F_3$, (x) $^5D_0 \rightarrow {}^7F_4$

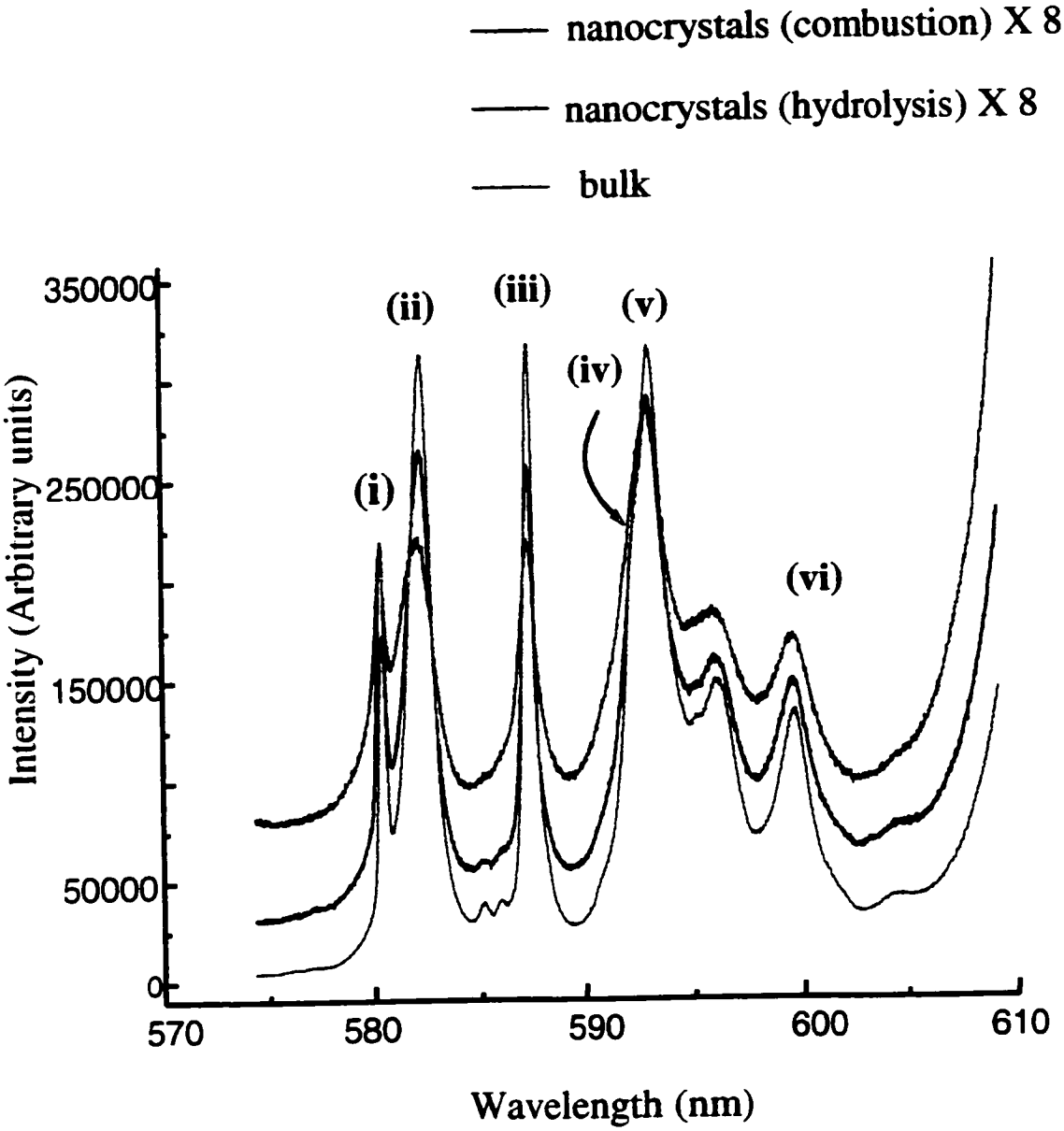

Figure 4.1.3: Room Temperature Emission of 1mol% Eu^{3+}:Y_2O_3 samples between 580-600nm, λ_{ex} =514.5nm; (i) $^5D_0 \rightarrow {}^7F_0(C_2)$, (ii) $^5D_0 \rightarrow {}^7F_{1a}(C_{3i})$, (iii) $^5D_0 \rightarrow {}^7F_{1a}(C_2)$, (iv) $^5D_0 \rightarrow {}^7F_{1b}(C_{3i})$, (v) $^5D_0 \rightarrow {}^7F_{1b}(C_2)$, (vi) $^5D_0 \rightarrow {}^7F_{1c}(C_2)$

Cubic Y_2O_3 crystallizes in the C bixbyite structure, with space group Ia3 (T_h^7) [45]. Y^{3+} ions occupy in the unit cell 24 sites with point symmetry C_2 and 8 sites with point symmetry C_{3i}. In general, Ln^{3+} ions have been found to be randomly distributed in both sites of Y_2O_3 as single crystals [15], although preferential occupation of the C_2 site has been suggested for Gd^{3+} and Eu^{3+} [29,30]. Due to an inversion center, *f-f* electric dipole transitions are forbidden for C_{3i} sites. Thus, the observed transitions are attributed to ions in C_2 symmetry sites (electric dipole allowed) and to the magnetic dipole allowed transitions from both the C_2 and C_{3i} sites, in addition to the vibronic C_{3i} transition.

Figure 4.1.4 shows the energy level diagram for the $Eu^{3+}(C_2)$ and $Eu^{3+}(C_{3i})$ ions which is in excellent agreement for Eu^{3+}:Y_2O_3 single crystals reported by Heber et al. [20]. As a result of their work, they calculated the $^7F_0$-$^7F_1$ energy distance ΔW_1 (C_{3i}) to be 132 ± 5cm^{-1} by measuring the temperature dependence of the absorption intensity of the line whereas, this thesis reports an energy distance of 127cm^{-1} from room temperature emission spectra of the Eu^{3+}:Y_2O_3 nanocrystals. Furthermore, Figure 4.1.4 assigns the energy spacing between the $^5D_0$ level of the C_{3i} sites to be ~90cm^{-1} higher in energy than the $^5D_0$ level of the C_2 sites. Since low Eu^{3+} concentrations were used in this study, weak lines occurring from the higher lying $^5D_1$ level to the $^7F_0$ ground state were observed. However, they have been shown to disappear upon increasing the Eu^{3+} concentrations due to rapid cross relaxation [37]. Only at concentrations less than 0.1 mol% are Eu^{3+} ions distant enough from each other so that no interaction takes place, causing there to exist two independent ion systems $Eu^{3+}(C_2)$ and $Eu^{3+}(C_{3i})$ where an energy transfer process becomes impossible between the two sites [31].

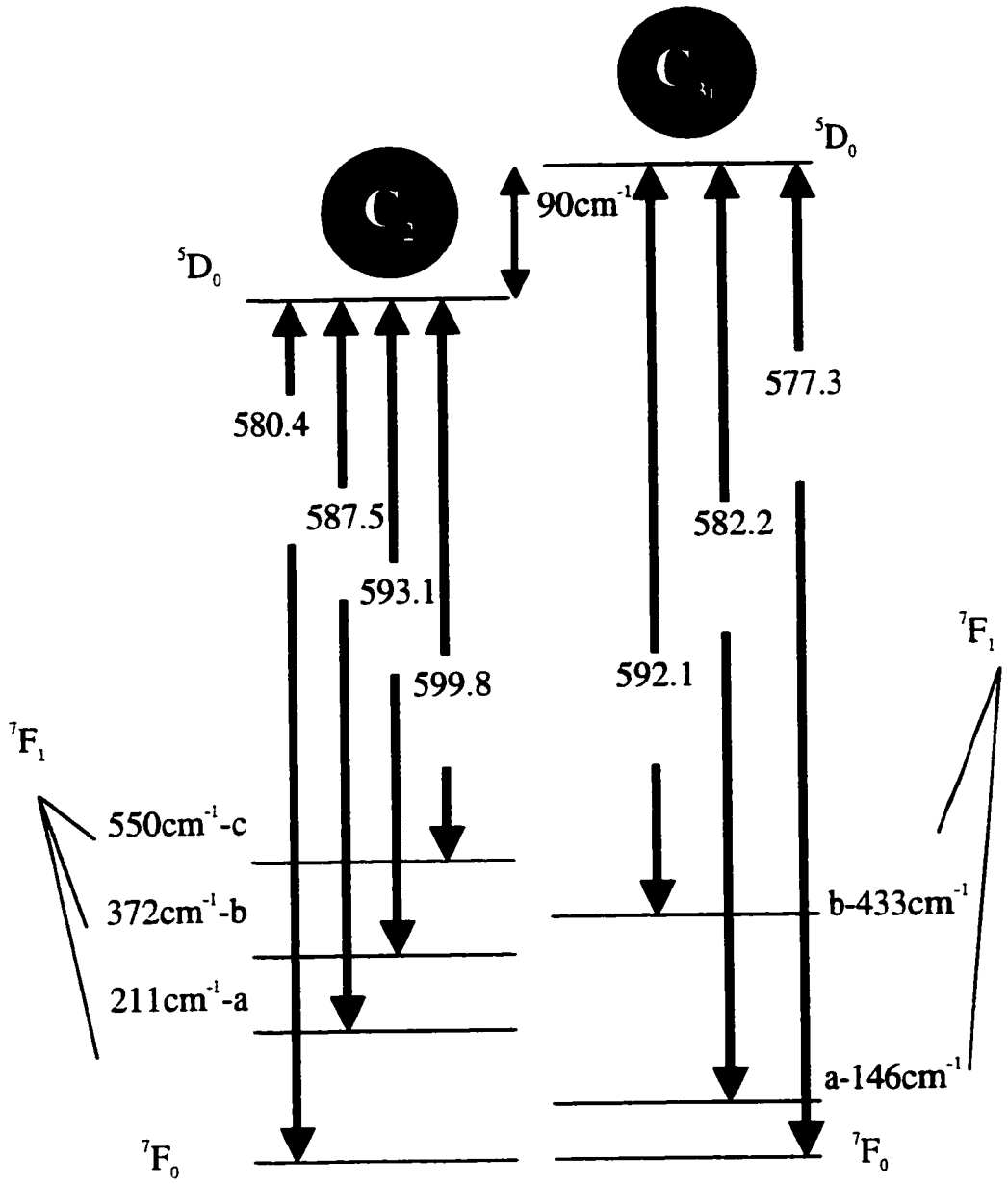

Figure 4.1.4: Energy Level Diagram of Eu^{3+}:Y_2O_3 Nanocrystal and Bulk Systems

4.2 ENERGY TRANSFER BETWEEN $Eu^{3+}(C_2)$ and $Eu^{3+}(C_{3i})$ IONS

The effect of C_2 and C_{3i} sites on the optical properties and energy transfer processes of Eu^{3+} doped Y_2O_3 nanocrystals has been the recent focus of research in materials science [16,19]. In the case of low Eu^{3+} concentrations in single crystals, energy transfer has been found to occur over more than 7Å between Eu^{3+} (C_{3i}) ions and Eu^{3+} (C_2) ions [20].

For this study, the 1.0 mol % Eu^{3+}doped Y_2O_3 nanocrystal samples prepared by hydrolysis and combustion methods in addition to the bulk sample were selectively excited at 580.0nm and 582.6nm corresponding to the $^5D_0(C_2)$ and $^5D_0(C_{3i})$ levels respectively. The 1mol% Eu^{3+}:Y_2O_3 samples were chosen for this energy transfer study since at higher concentrations rapid cross-relaxation causes signal quenching. Signal quenching causes C_2-type emission to dominate the spectra masking emission from the weaker C_{3i} sites as shown in Figure 4.2.1. This poses a problem when it becomes necessary to distinguish between C_{3i} and C_2 emission for Eu^{3+} ions. Emission from these two levels was monitored at 298K and 77K, in order to determine the effect of temperature on energy transfer. Site selective spectroscopy contributes to the understanding of the structure, phase distribution, crystallinity, phonon spectrum, electron-phonon interactions and dopant chemistry in nanostructured materials [33]. Thus, within the $^7D_0 \rightarrow {}^5F_1$ region, a distinction can be made between the transitions associated with the Eu^{3+} ions in the different sites (C_{3i},C_2).

Figures 4.2.2.1 through 4.2.4.1 inclusively show that excitation into the two different crystallographic sites produced distinct emission spectra for both the nanocrystal and bulk samples. The black lines in both figures represent the emission observed upon excitation at 580.0nm into the $^5D_0$ level of C_2 sites. Emission at 298K for the nanocrystal and bulk samples consisted of the weak $^5D_0 \rightarrow {}^7F_{1a}(C_{3i})$ line indicating a back transfer of energy from the $^5D_0(C_2)$ level to the $^5D_0(C_{3i})$ over the energy gap determined to be ~90cm^{-1} according to spectral data. Unlike other lattices, the two sites in Y_2O_3 are significantly different causing an observable energy difference between the $^5D_0$ levels of the Eu^{3+} ion [37]. Thus, one would assume that the probability of back transfer in Y_2O_3 from Eu^{3+} ions in C_2 sites to Eu^{3+} ions in C_{3i} sites to be unlikely. However, the energy transfer from the C_2 to C_{3i} site becomes possible because the energy difference between the $^5D_0$ levels can be bridged thermally at room temperature [46]. In addition to $Eu^{3+}(C_{3i})$ lines, the following emission lines were also observed for $Eu^{3+}(C_2)$ ions: $^5D_0 \rightarrow {}^7F_{1a}$, $^5D_0 \rightarrow {}^7F_{1b}$, and $^5D_0 \rightarrow {}^7F_{1c}$.

The red traces in Figures 4.2.2.1 through 4.2.4.2 show the emission spectra upon excitation at 582.2nm within the $^5D_0 \rightarrow {}^7F_{1a}$ manifold for C_{3i} sites. Intense C_2-type emission at ~611nm ($^5D_0 \rightarrow {}^7F_2$) was observed providing evidence that upon excitation at 582.2nm, a forward energy transfer process occurs from the $^5D_0$ level of Eu^{3+} in the C_{3i} sites to Eu^{3+} ions in C_2 sites. At this point, it seems that Eu^{3+} ions have successfully substituted both Y^{3+} sites, as shown by this two-way energy transfer process between the $^5D_0$ level of C_{3i} and C_2 sites. This confirms what was previously postulated by Hunt et al. [48], that the emission efficiency of Eu^{3+}:Y_2O_3 samples is not hindered by the presence of

significantly different sites. As shown in previous single crystal work by Hunt et al. [48], the emission between 592-600 nm is more complex when exciting into C_{3i} sites, since energy transfer from the $^5D_0$ (C_{3i}) level to the $^5D_0(C_2)$ level, is a superposition of both C_2 and C_{3i}-type emission [48].

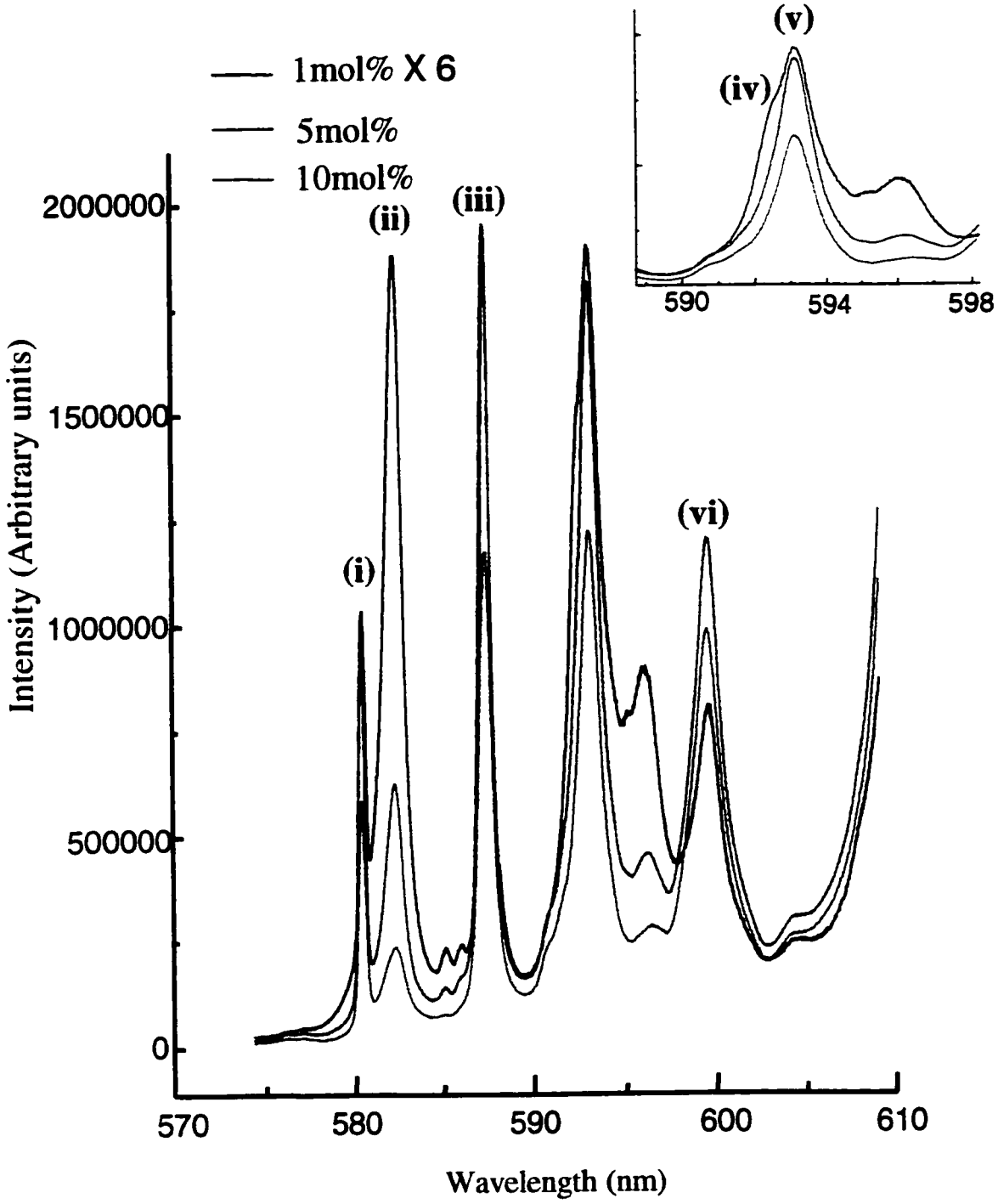

Figure 4.2.1: Comparison of Room Temperature Emission for 1, 5 and 10mol% Eu^{3+}:Y_2O_3 Bulk Samples, λ_{ex}=514.5nm; (i) $^5D_0 \rightarrow {}^7F_0(C_2)$, (ii) $^5D_0 \rightarrow {}^7F_{1a}(C_{3i})$, (iii) $^5D_0 \rightarrow {}^7F_{1a}(C_{3i})$, (iv) $^5D_0 \rightarrow {}^7F_{1b}(C_2)$, (v) $^5D_0 \rightarrow {}^7F_{1b}(C_2)$, (vi) $^5D_0 \rightarrow {}^7F_{1c}(C_2)$

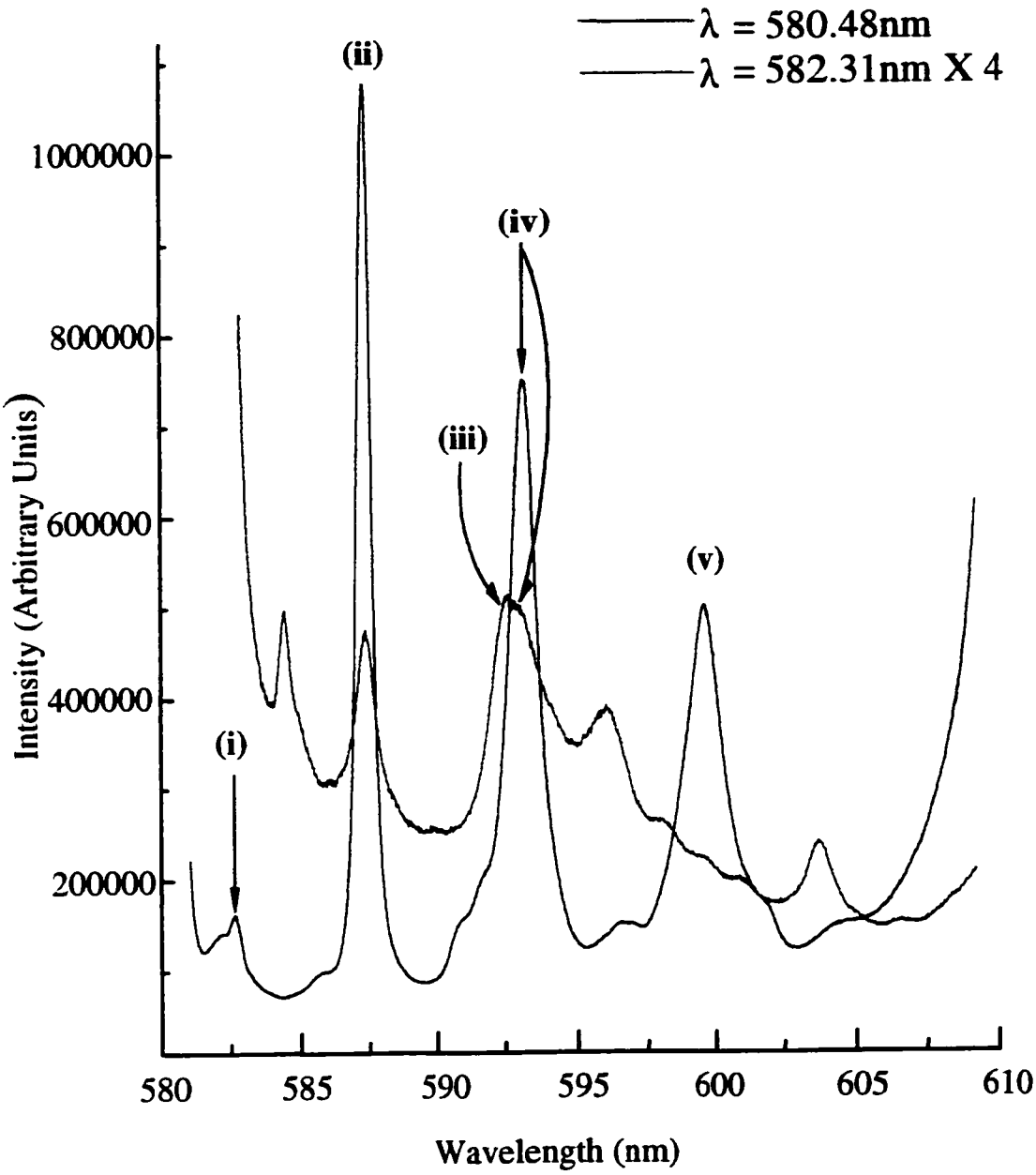

Figure 4.2.2.1: Site Selective Room Temperature Emission of 1mol% Eu^{3+}:Y_2O_3 Nanocrystals (Combustion); (i) $^5D_0 \rightarrow {}^7F_{1a}(C_{3i})$, (ii) $^5D_0 \rightarrow {}^7F_{1a}(C_2)$, (iii) $^5D_0 \rightarrow {}^7F_{1b}(C_{3i})$, (iv) $^5D_0 \rightarrow {}^7F_{1b}(C_2)$, (v) $^5D_0 \rightarrow {}^7F_{1c}(C_2)$

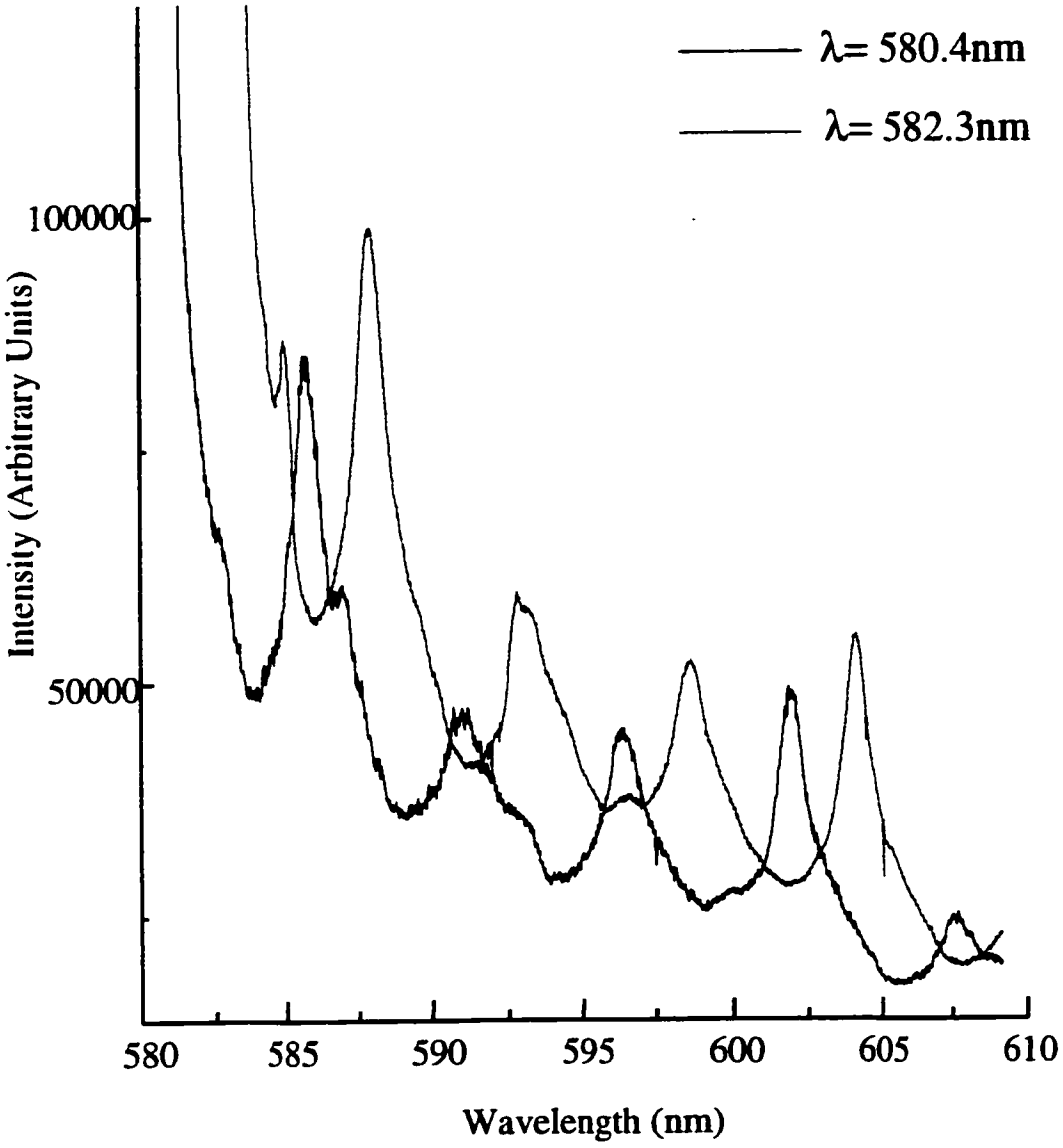

Figure 4.2.2.2: Site Selective Low Temperature Emission (77°K) of 1mol% Eu^{3+}:Y_2O_3 Nanocrystals (Combustion)

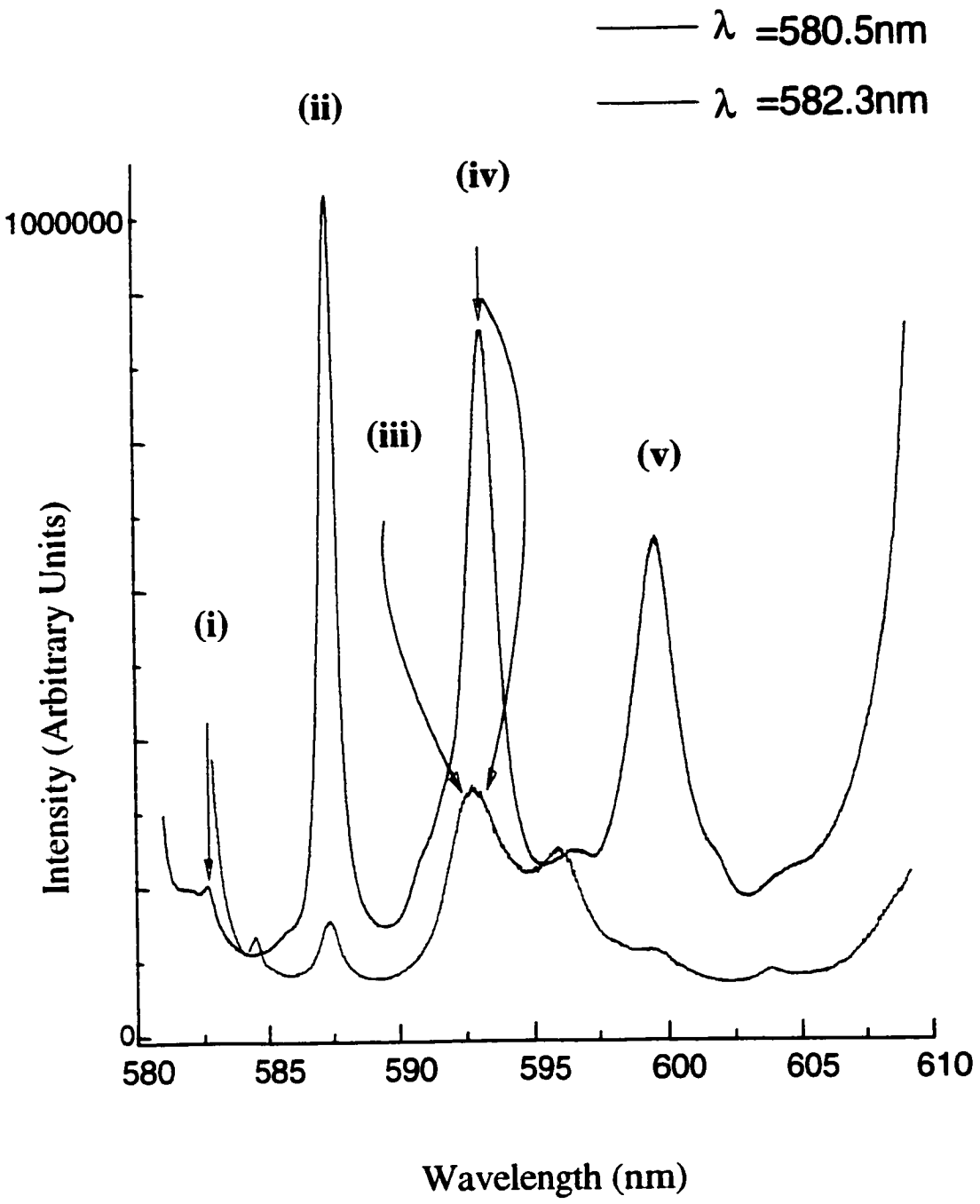

Figure 4.2.3.1: Site Selective Room Temperature Emission of 1mol% Eu^{3+}:Y_2O_3 Nanocrystals (Hydrolysis); (i) $^5D_0 \rightarrow {}^7F_{1a}(C_{3i})$, (ii) $^5D_0 \rightarrow {}^7F_{1a}(C_2)$, (iii) $^5D_0 \rightarrow {}^7F_{1b}(C_{3i})$, (iv) $^5D_0 \rightarrow {}^7F_{1b}(C_2)$, (v) $^5D_0 \rightarrow {}^7F_{1c}(C_2)$

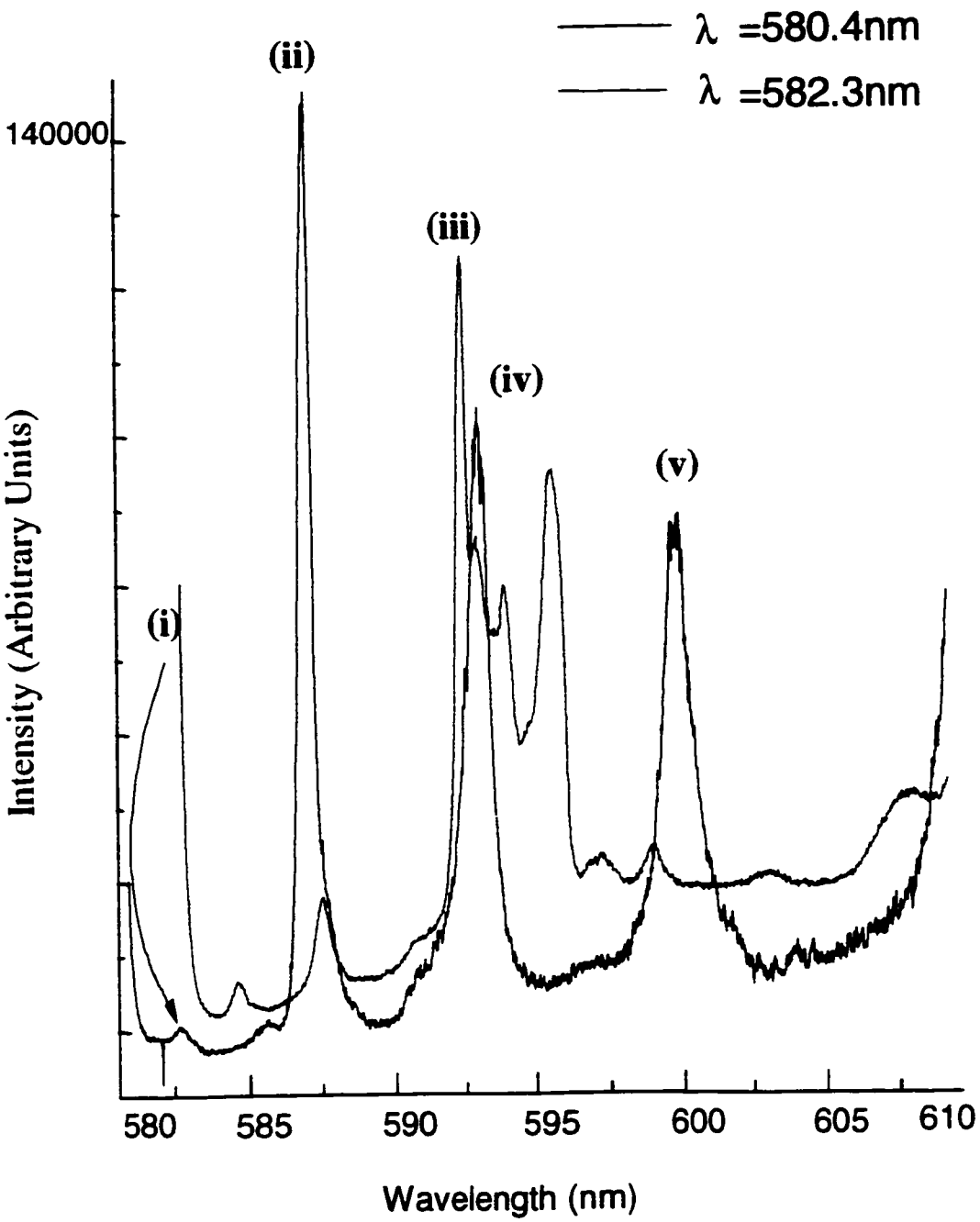

Figure 4.2.3.2: Site Selective Low Temperature Emission (77°K) of 1mol% Eu^{3+}:Y_2O_3 Nanocrystals (Hydrolysis); (i) $^5D_0 \rightarrow {}^7F_{1a}(C_{3i})$, (ii) $^5D_0 \rightarrow {}^7F_{1a}(C_2)$, (iii) $^5D_0 \rightarrow {}^7F_{1b}(C_{3i})$, (iv) $^5D_0 \rightarrow {}^7F_{1b}(C_2)$, (v) $^5D_0 \rightarrow {}^7F_{1c}(C_2)$

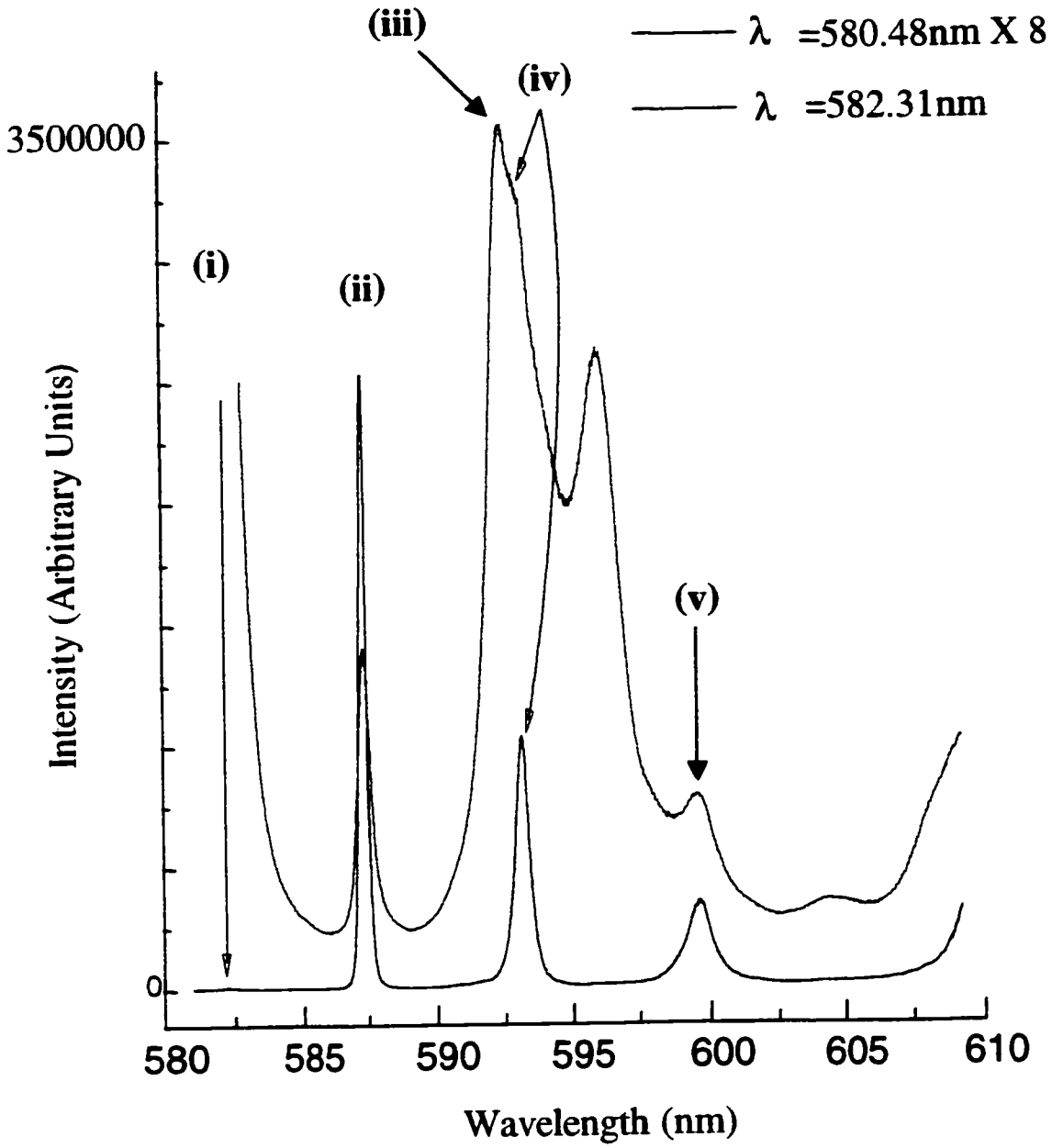

Figure 4.2.4.1: Site Selective Room Temperature Emission of 1mol% Eu^{3+}:Y_2O_3 Bulk Sample; (i) $^5D_0 \rightarrow {}^7F_{1a}(C_{3i})$, (ii) $^5D_0 \rightarrow {}^7F_{1a}(C_2)$, (iii) $^5D_0 \rightarrow {}^7F_{1b}(C_{3i})$, (iv) $^5D_0 \rightarrow {}^7F_{1b}(C_2)$, (v) $^5D_0 \rightarrow {}^7F_{1c}(C_2)$

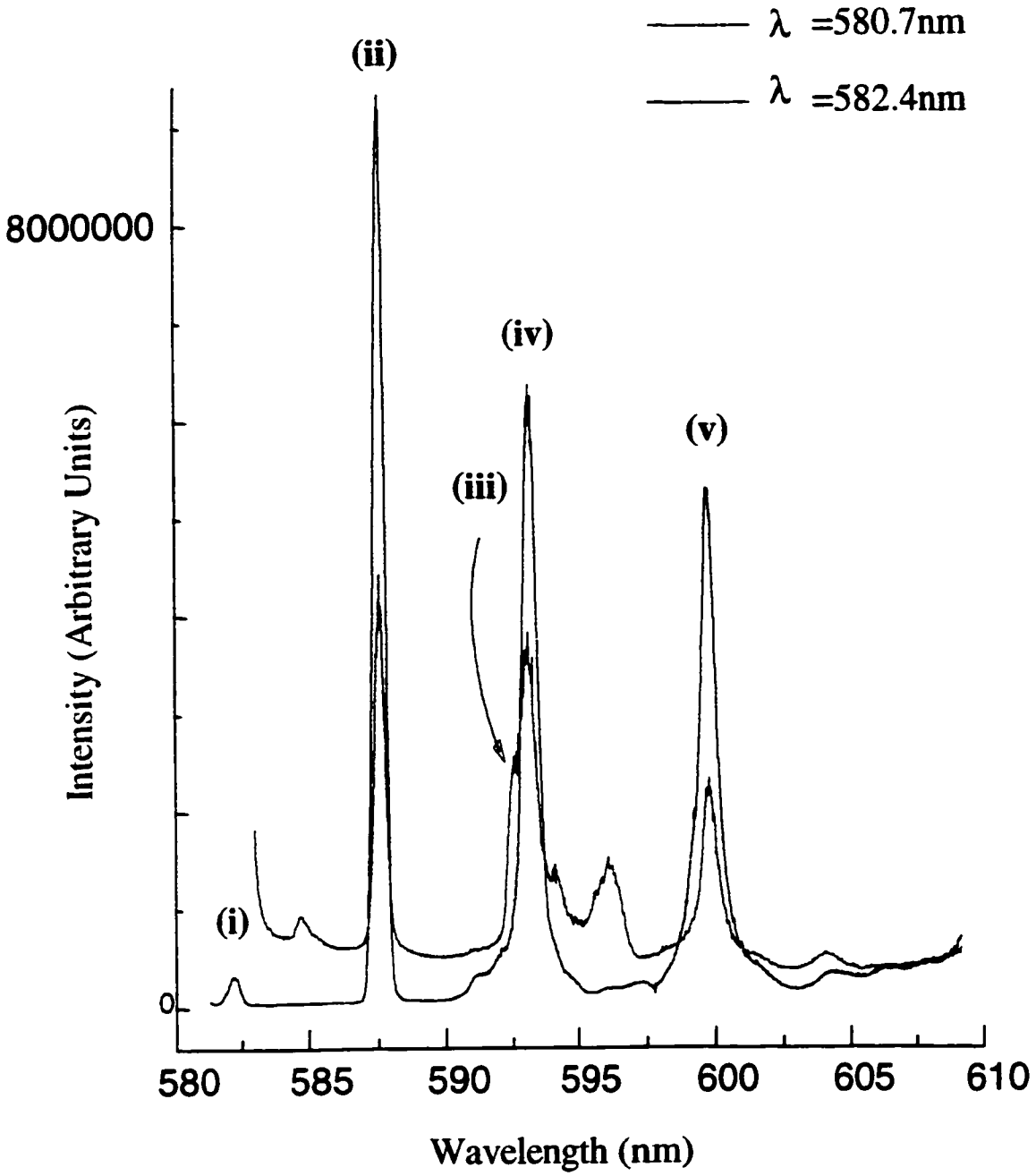

Figure 4.2.4.2: Site Selective Low Temperature Emission (77°K) of 1mol% Eu^{3+}:Y_2O_3 Bulk Sample; (i) $^5D_0 \rightarrow {}^7F_{1a}(C_{3i})$, (ii) $^5D_0 \rightarrow {}^7F_{1a}(C_2)$, (iii) $^5D_0 \rightarrow {}^7F_{1b}(C_{3i})$, (iv) $^5D_0 \rightarrow {}^7F_{1b}(C_2)$, (v) $^5D_0 \rightarrow {}^7F_{1c}(C_2)$

Site selective work was carried out at 77K in order to study the effect of temperature on the energy transfer process from $Eu^{3+}(C_{3i})$ to $Eu^{3+}(C_2)$. From the spectral data obtained, it is evident that energy transfer is efficient even at low temperatures as indicated by the intense C_2 emission peak at ~611nm corresponding to $^5D_0 \rightarrow {}^7F_2$ hypersensitive transition of C_2 sites. Emission spectra for the nanocrystals has confirmed what was observed by Heber et al. [20] in single crystals, that energy transfer is efficient at low temperature, and even more efficient at room temperature. Due to the presence of a center of inversion, only magnetic dipole transitions (Selection rule $\Delta J=0, \pm 1$, $J=0 \rightarrow J=0$ forbidden) are allowed for $Eu^{3+}(C_{3i})$ ion [46]. In addition to the magnetic dipole transitions, $Eu^{3+}(C_2)$ ions show forced electric dipole transitions [46]. The site selective work focused on developing a better understanding of the influence of C_2 and C_{3i} sites on the emission of Eu^{3+} in the $^5D_0 \rightarrow {}^7F_0$ and $^5D_0 \rightarrow {}^7F_1$ region for $Eu^{3+}:Y_2O_3$ nanocrystals.

However, there are certain differences between the emission spectra obtained at 298K versus 77K for the nanocrystals samples specifically. At 77K the 1mol% $Eu^{3+}:Y_2O_3$ nanocrystal combustion sample expressed an evident red shift of all emission lines in comparison to emission data collected at 298K as shown in Figure 4.2.2.2. This red shift can be attributed to a large degree of disorder in the local environment of the probe ion incurred during the sample preparation method especially when yielding particle sizes below 300Å [49,50]. The disorder could be structural disorder throughout the particles, disorder due to oxygen vacancies, or surface disorder [51]. This phenomenon has been shown to occur often with $Eu^{3+}:Y_2O_3$ samples prepared by the combustion technique [51]. Diffuse reflectance experiments confirmed this same red

shift in the charge transfer band for Eu^{3+}:Y_2O_3 combustion nanocrystals in comparison to the Eu^{3+}:Y_2O_3 hydrolysis nanocrystals as shown in Figure 4.2.5.

The emission spectra for the 1mol% Eu^{3+}:Y_2O_3 hydrolyzed nanocrystals was far more resolved at 77K since vibrations from water molecules were eliminated at such low temperature. Overall, emission intensities at 77K were higher as was the vibronic C_{3i} transition at 596nm. Bending and stretching of the H-O-H matrix is prominent since as a side effect of the preparation method, residual water molecules imbed themselves in the holes or pockets within the crystal lattice of the nanocrystals during their growth [52].

In this study, sufficient evidence was obtained for the energy transfer process between $Eu^{3+}(C_{3i})$ and $Eu^{3+}(C_2)$ ions for Eu^{3+}:Y_2O_3 nanocrystals. Thus, we can conclude at this stage that Eu^{3+} ions do not express preferential occupation towards either C_2 or C_{3i} sites. This in turn, will not significantly impact the efficiency of the Eu^{3+} when doped in Y_2O_3, since intense C_2-type emission at 611nm was observed upon both C_{3i} and C_2 excitation at 582.2 and 580.0nm respectively.

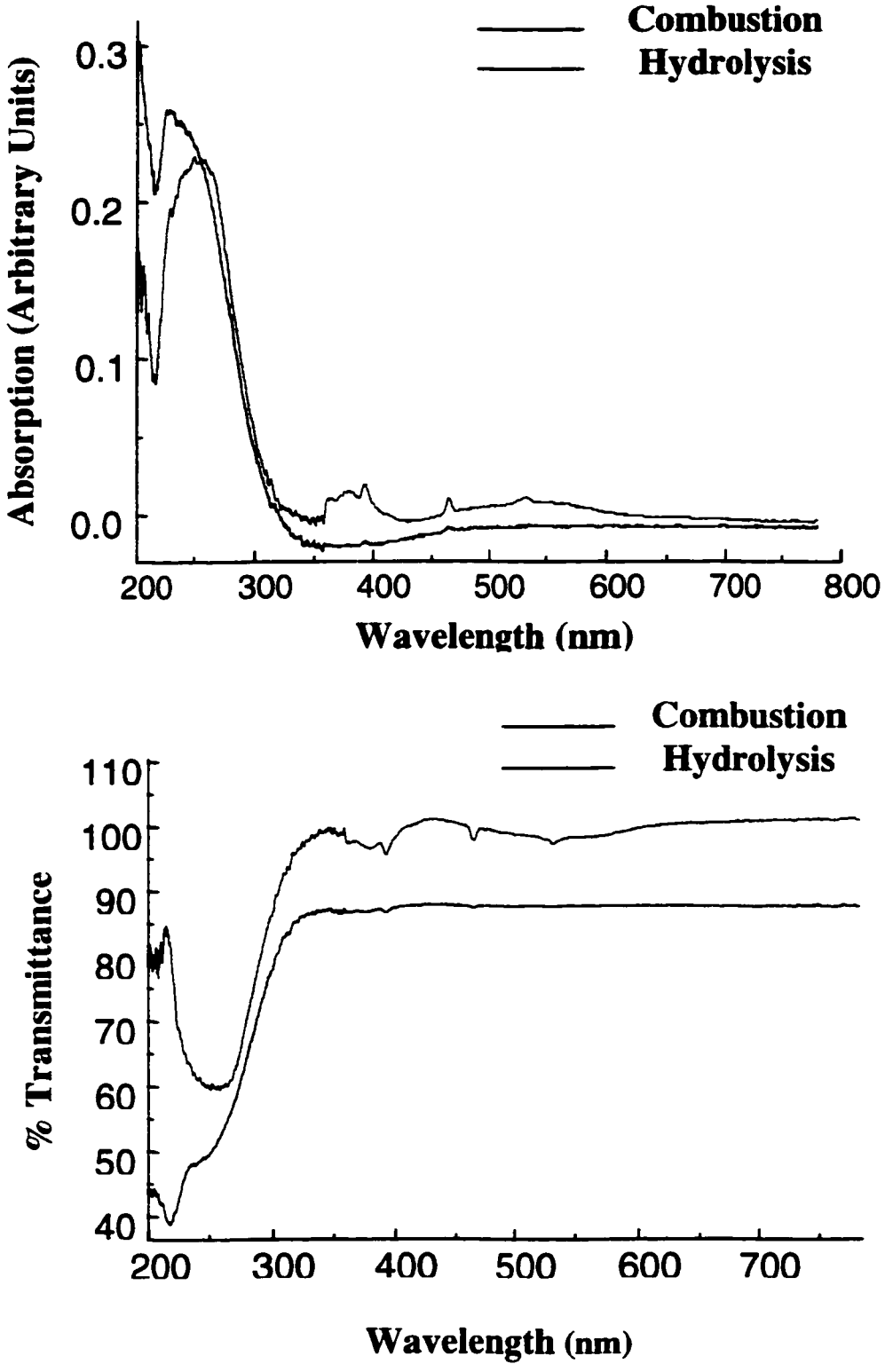

Figure 4.2.5: Room Temperature Diffuse Reflectance of 10mol% Eu^{3+}:Y_2O_3 Nanocrystals

4.3 LIFETIME AND TRANFER RATES FROM $Eu^{3+}(C_{3i})$ to $Eu^{3+}(C_2)$

The lifetime for the $^5D_0$ level for the Eu^{3+} ions in the C_2 sites was monitored at 611nm ($^5D_0 \rightarrow {}^7F_2$) at 298K and 77K. Direct excitation at 580.0nm produced single exponential curves with decay constants for the $^5D_0 \rightarrow {}^7F_2$ (C_2) transition of 2.2ms and 2.0ms for the 1mol% $Eu^{3+}:Y_2O_3$ combustion and hydrolysis and sample respectively. The double exponential obtained for the 1mol% bulk sample may be caused by a second order rate process influenced by rapid cross-relaxation mechanisms more evident when dealing with larger particle sizes such as with the bulk sample. In comparison to C_2 excitation, excitation into the C_{3i} site at 582.2nm, produced a longer lifetime on the order of 1.5, since the later is both magnetic and electric dipole forbidden according to the selection rules [46]. Figures 4.3.1 and 4.3.2 show the room temperature decay curves for the $^5D_0 \rightarrow {}^7F_2$ transition for $Eu^{3+}:Y_2O_3$ nanocrystals prepared via the combustion method following excitation at 580.0nm 582.2nm respectively.

Table 4.3.1 compares the decay times obtained for the various 1mol% samples at 298K and 77K by monitoring the $^5D_0 \rightarrow {}^7F_2(C_2)$ transition following direct excitation into the $^5D_0$ level of C_2 and C_{3i} sites independently.

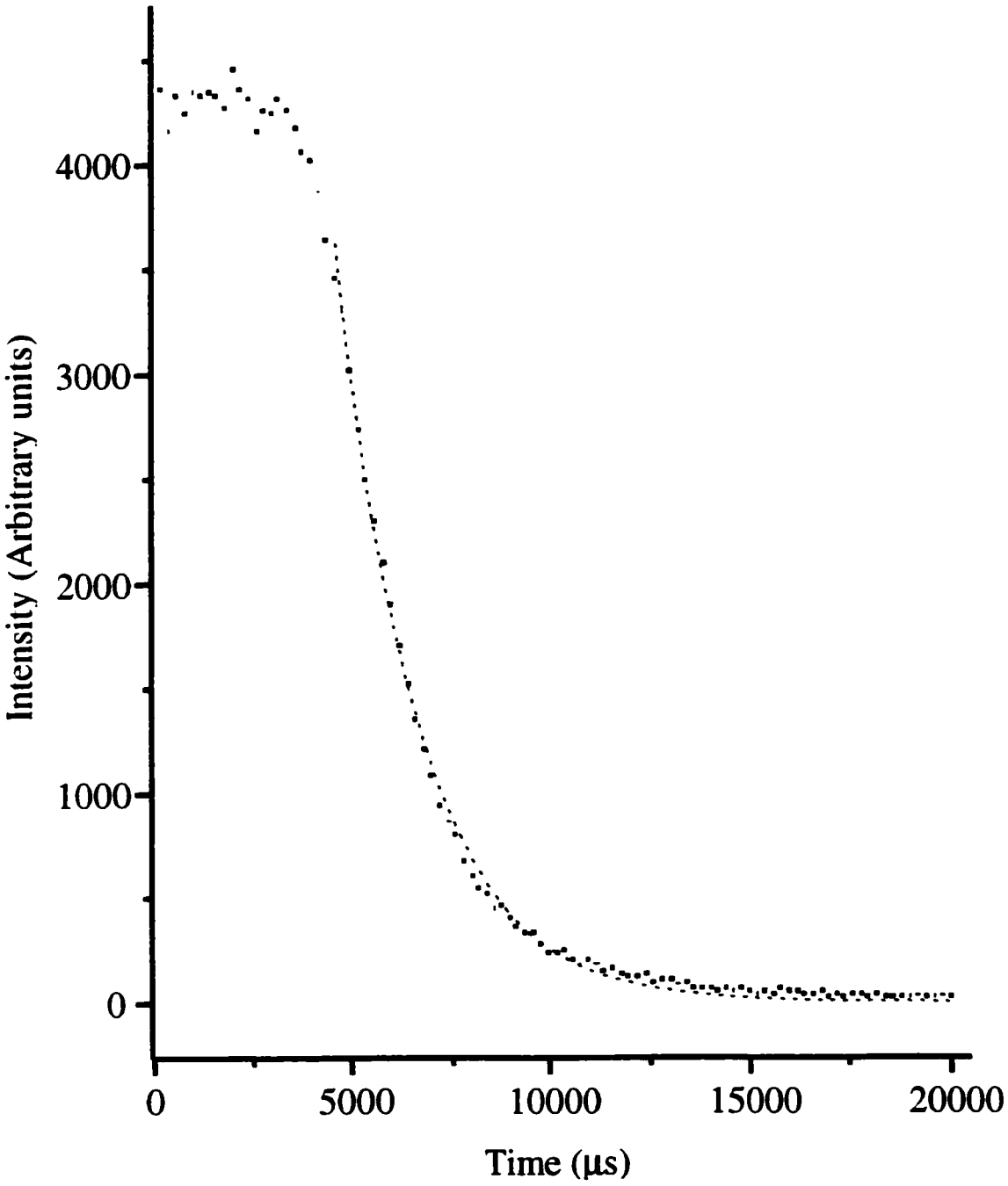

Figure 4.3.2: Room Temperature Lifetime of the $^5D_0 \rightarrow {}^7F_2$ (C_2) transition for the 1mol% Eu^{3+}:Y_2O_3 Nanocrystal (Combustion) sample following excitation into C_2 sites, λ_{ex}=580.2nm

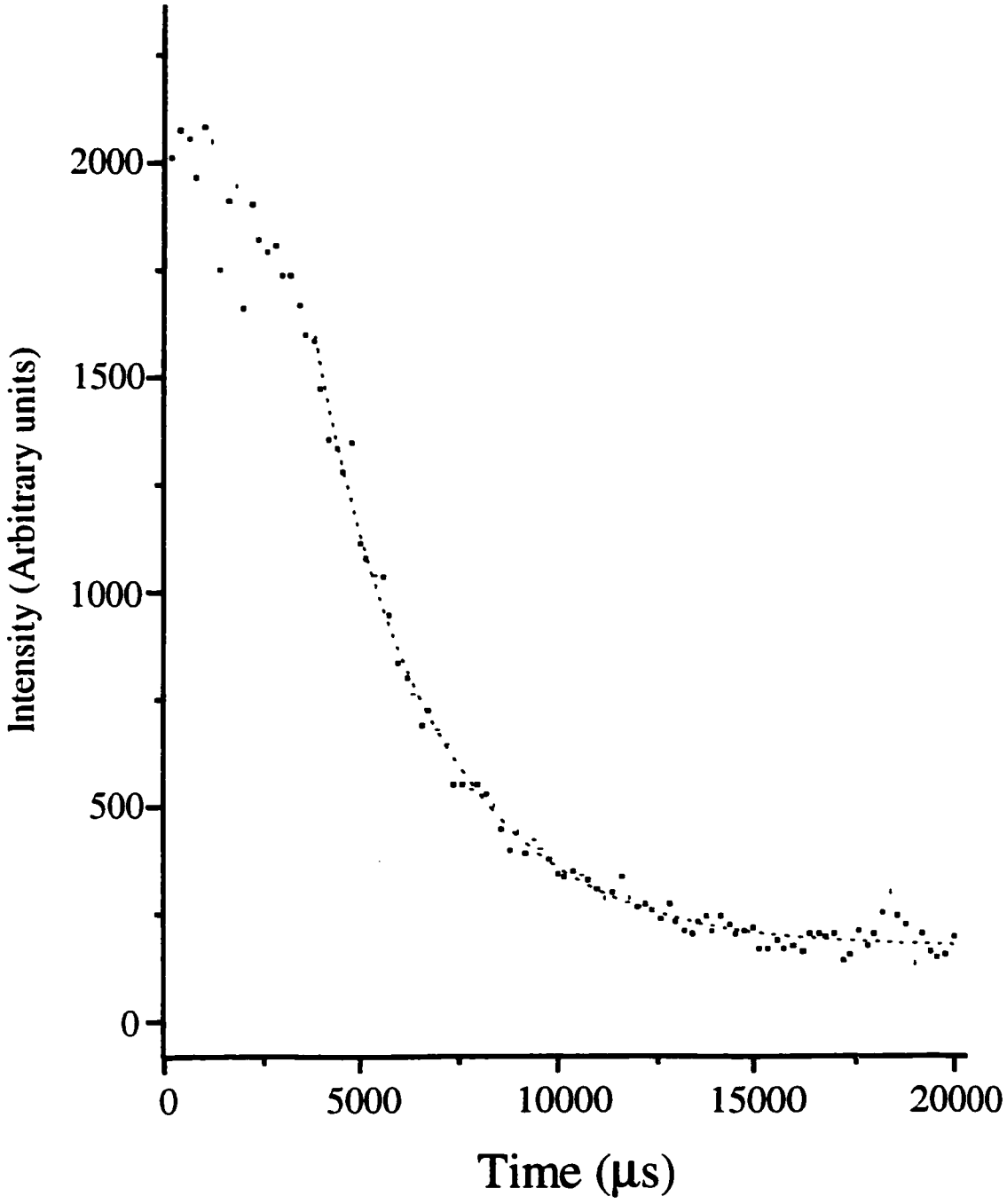

Figure 4.3.3: Room Temperature Lifetime of the $^5D_0 \rightarrow {}^7F_2$ (C_2) transition for the 1mol% Eu^{3+}:Y_2O_3 Nanocrystals (Combustion) sample following excitation into C_{3i} sites, λ_{ex}=582.4nm

Table 4.3.1 Fluorescence Lifetimes of the $^5D_0 \rightarrow {}^7F_2(C_2)$ for the 1mol% $Eu^{3+}:Y_2O_3$ samples

	C_2 Excitation at 298K (ms)	C_{3i} Excitation at 298K (ms)	C_2 Excitation at 77K (ms)	C_{3i} excitation at 77K (ms)
Combustion	2.2	3.5	1.6	2.5
Hydrolysis	2.0	1.6,4.8	1.7	2.0
Bulk	1.4,3.5	1.7,8.6	1.1	1.3

The decay rate τ^{-1}, contains both radiative and non-radiative components. The excited state of a specific ion decays exponentially with a certain lifetime τ, yielding the total decay rate given by the following relationship:

$$1/\tau_{obs} = 1/\tau_{rad} + 1/\tau_{non\text{-}rad} \qquad 4.3.1$$

At low dopant concentrations, the fluorescence lifetimes exhibit exponential decay. However, at high Eu^{3+} concentrations, donor-donor interactions will induce a deviation from exponential decay. Since low dopant concentrations of 1mol% $Eu^{3+}:Y_2O_3$ were used in this study, signal quenching can be ignored. Evaluations of fluorescence lifetimes are very useful since they provide information on the transition probability. Studies have shown that the probability of a transition varies proportionally with decay rate [53].

Figures 4.3.3 and 4.3.4 show the linear relationship between the log of intensity and decay time, where the slope corresponds to the decay rate with units of inverse time. The ratio of the decay rates is $0.0002\mu s^{-1}/0.00009\mu s^{-1}$ or 2:1 for $^5D_0(C_2)/^5D_0(C_{3i})$ levels. These rate constants confirm that an energy transfer step is involved from $Eu^{3+}(C_{3i})$ to $Eu^{3+}(C_2)$. Thus, the lifetime of the $^5D_0$ level for the C_2 site lengthens with C_{3i} excitation. Therefore, it is evident from the lifetime studies that two distinct sites are contributing to emission spectra and the probability of a transition involving a $Eu^{3+}(C_2)$ ion is twice as much as one involving a $Eu^{3+}(C_{3i})$ ion. This is consistent with the spectral data obtained and known selection rules. Since emission is dominated by the C_2 site for the $^5D_0 \rightarrow {}^7F_2$ transition, then the rate associated with the transfer from $^5D_0$ level of $Eu^{3+}(C_{3i})$ is small thereby causing the probability of a transition occurring from that level to be equally low.

Furthermore, the lifetime for $^5D_0(C_2)$ level was shorter following excitation at 580nm for all three samples at low temperature. This could only be possible if the two-way energy transfer step no longer exists or becomes fairly weak at 77K, thereby preventing the $^5D_0(C_2)$ population from feeding the $^5D_0(C_{3i})$ level, thus increasing the rate of emission from the $^5D_0(C_2)$ level.

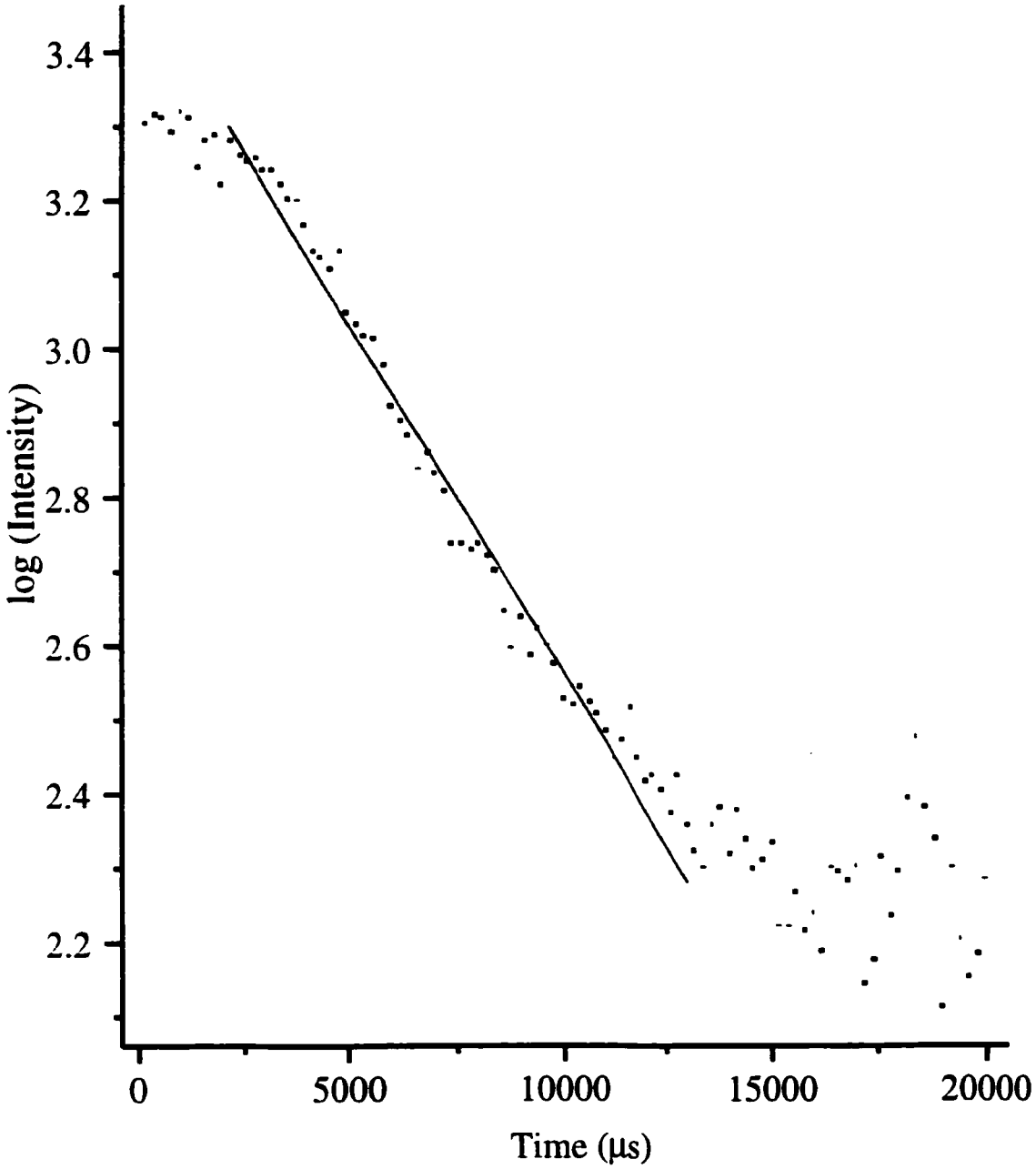

Figure 4.3.3: Transfer Rate of the $^5D_0 \rightarrow {}^7F_2$ (C_2) transition of 1mol% Eu^{3+}:Y_2O_3 Nanocrystal (Combustion) Sample following excitation into C_{3i} sites, λ_{ex}=582.4nm

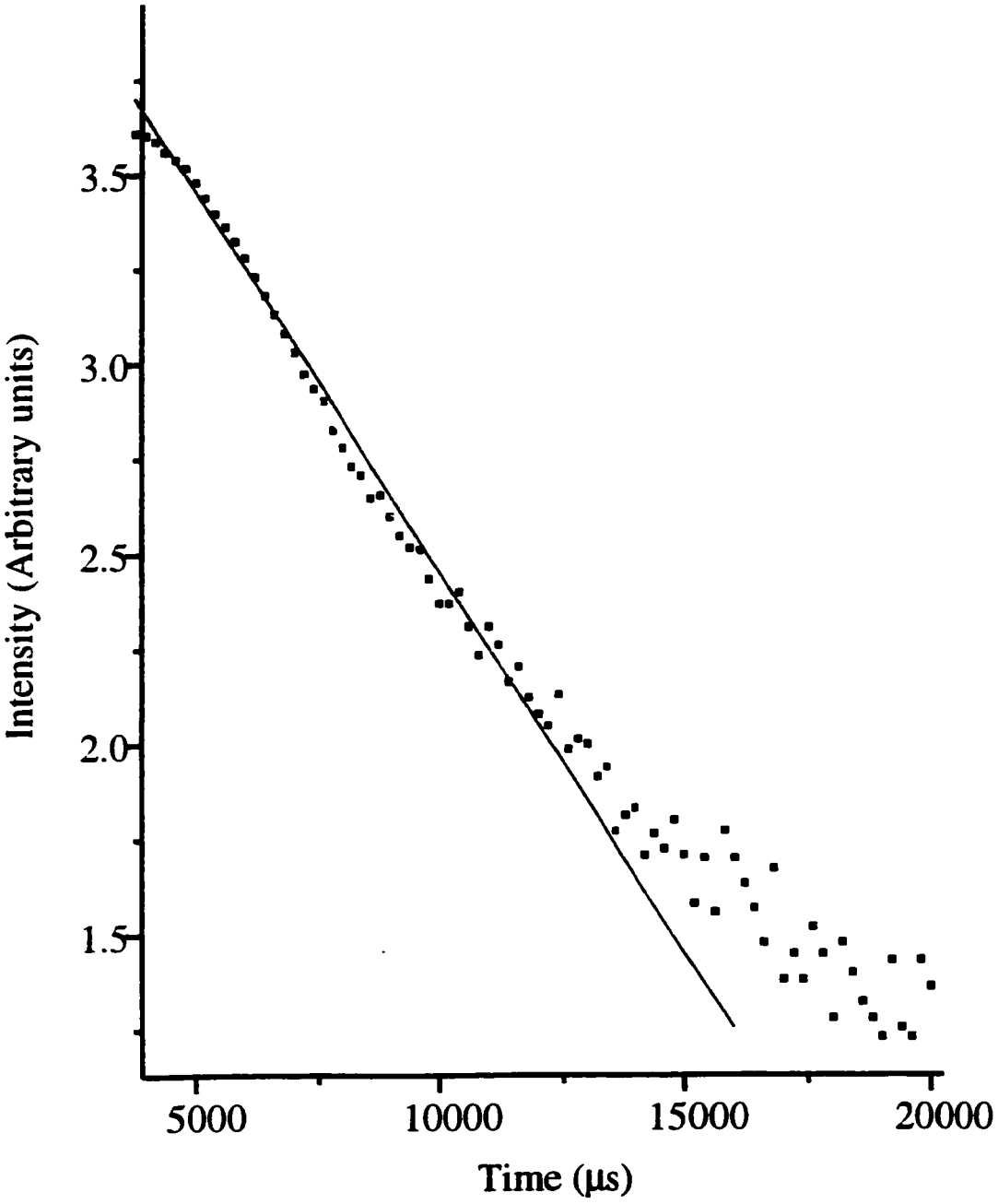

Figure 4.3.4: Transfer Rate of the $^5D_0 \rightarrow {}^7F_2$ (C_2) transition of 1mol% Eu^{3+}:Y_2O_3 Nanocrystal (Combustion) Sample following excitation into C_2 sites, λ_{ex}=580.2nm

4.4 TEMPERATURE DEPENDENCE OF THE $^5D_0$ LEVEL

The temperature dependence of the $^5D_0 \rightarrow {}^7F_0(C_2)$ versus the $^5D_0 \rightarrow {}^7F_{1a}(C_{3i})$ transition is shown in Figure 4.4.1 for the 1mol% bulk sample. An increase in the intensity of the $^5D_0 \rightarrow {}^7F_0(C_2)$ transition was observed as the temperature was lowered from 298K to 77K. This observation was accompanied with an increase in the intensity of the $^5D_0 \rightarrow {}^7F_{1a}(C_{3i})$ transition, due to the depopulation of the $^5D_0(C_2)$, feeding level for the energy transfer process.

An analysis based on a simple two–level thermalization process predicts that the thermalization of the higher lying energy state may be expressed by the following equation [54].

$$I_{1b}/I_{1a} = \rho^r{}_{1b}\eta_{1b}\omega_{1b}/\rho^r{}_{1a}\eta_{1a}\omega_{1a} \exp(-E_{1b1a}/kT) \qquad 4.4.1$$

where $\rho^r{}_{1a}$ and $\rho^r{}_{1b}$ are the total spontaneous-emission rates, $\eta\omega_{1a}$ and $\eta\omega_{1a}$ are the photon energies, g_{1a} and g_{1b} are the degeneracies (2J+1) of the $^5D_0(C_2)$ and $^5D_0(C_{3i})$ levels respectively, and I_{1a} and I_{1b} are the integrated intensities of the $^5D_0 \rightarrow {}^7F_0(C_2)$ and $^5D_0 \rightarrow {}^7F_{1a}(C_{3i})$. The E_{1b1a} term represents the energy gap between the $^5D_0(C_2)$ and $^5D_0(C_{3i})$ levels, k is the Boltzmann constant, and T is the temperature in degrees Kelvin. The photon energies of the two levels are similar and may be considered to be equal.

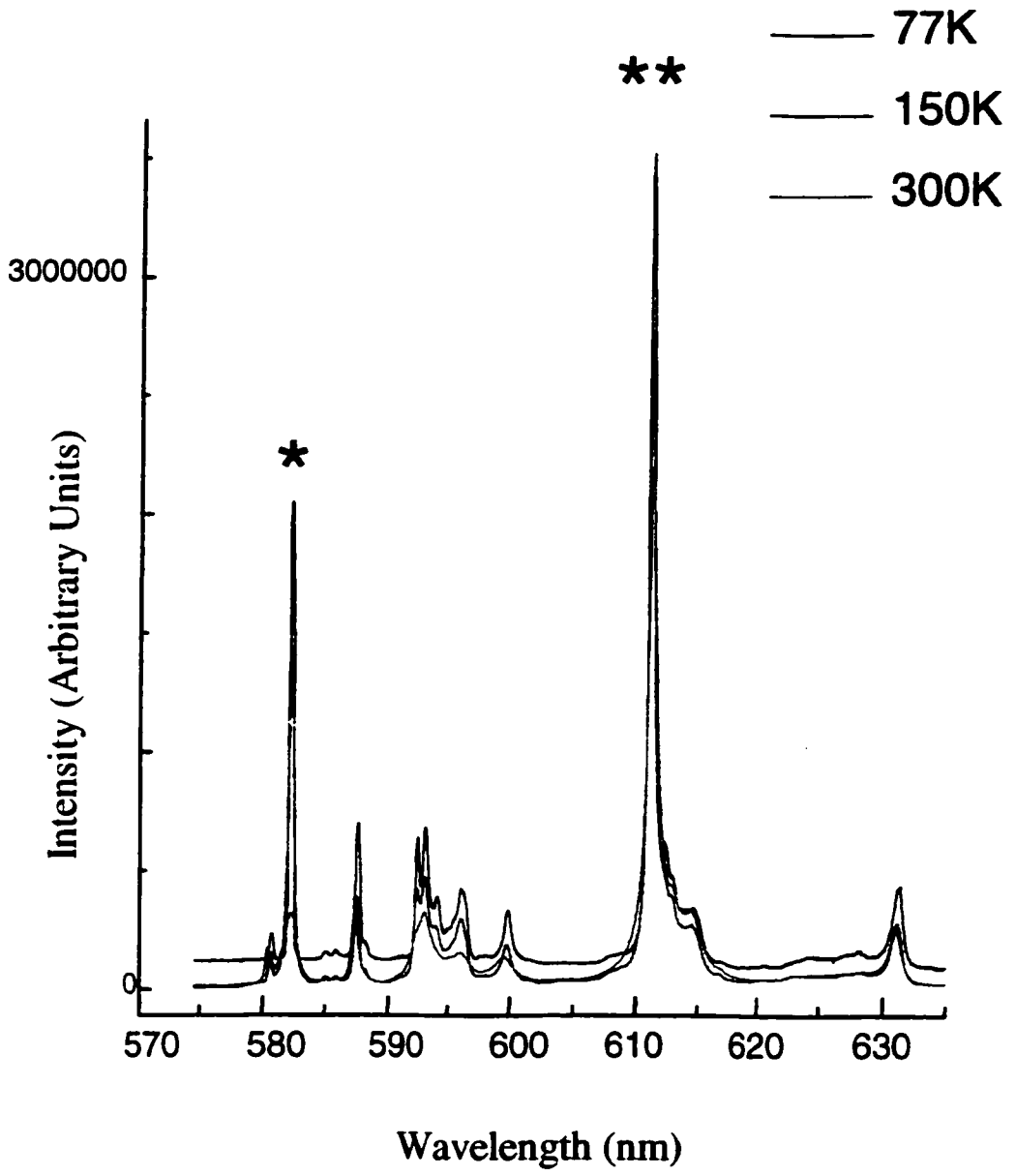

Figure 4.4.1: Temperature Dependence of Red Emission for 1mol% Eu^{3+}:Y_2O_3 Bulk Sample, λ_{ex}=514.5nm; $^{*5}D_0 \rightarrow {}^7F_{1a}(C_{3i})$ and $^{**5}D_0 \rightarrow {}^7F_2(C_2)$

A plot of the logarithm of the ratios of the integrated intensities for the transitions $^5D_0 \rightarrow {}^7F_0(C_2)$ and $^5D_0 \rightarrow {}^7F_{1a}(C_{3i})$ as a function of 1/T is shown in Figure 4.4.2. The thermal population of the $^5D_0(C_2)$ level was found to obey the Boltzmann distribution for the two level thermalization process (equation 4.5.1) between 298K and 150K, after which linearity was lost. The slope of the line between 298K and 150K corresponds to an energy gap of $82cm^{-1}$. This value is in excellent agreement with the experimental value ($\Delta E=90cm^{-1}$) determined from spectra.

Transitions originating from the $^5D_0(C_2)$ level are clearly visible at temperatures higher than 77K. At higher temperatures, the energy gap of approximately $90cm^{-1}$ from the lower lying $^5D_0(C_2)$ state can be easily bridged by low energy phonons or thermal vibrations. Thermalization of the $^5D_0(C_{3i})$ state has been observed in previous work by Heber et al. [20] on $Eu^{3+}:Y_2O_3$ single crystals and confirmed with this temperature dependence study of $Eu^{3+}:Y_2O_3$ nanocrystals.

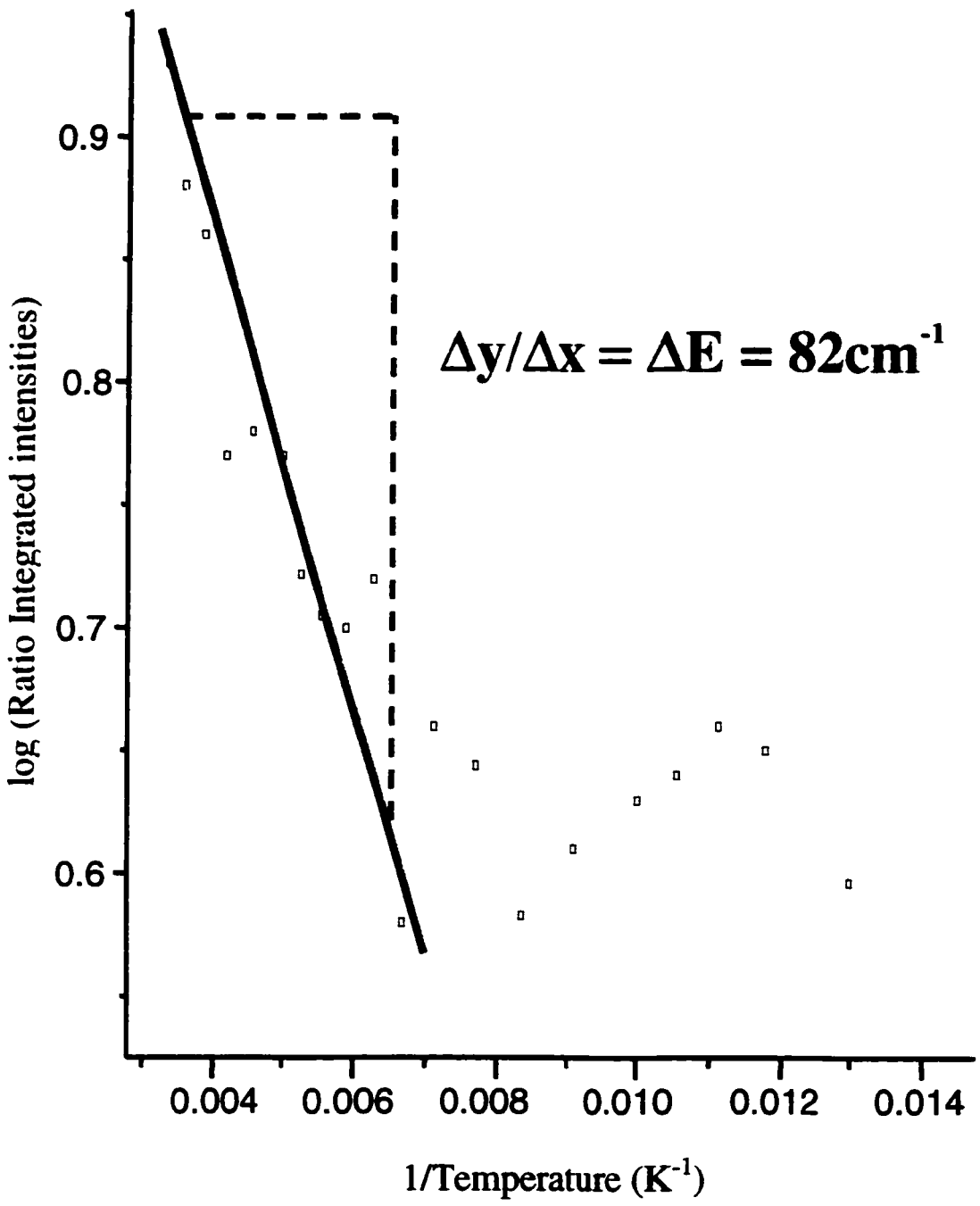

Figure 4.4.2 : Logarithm of Integrated Intensities [$^5D_0 \rightarrow {}^7F_{1a}(C_{3i})/{}^5D_0 \rightarrow {}^7F_2(C_2)$] as a Function of 1/Temperature

4.5 ELECTRONIC RAMAN SCATTERING AND I.R. LATTICE VIBRATIONS OF POWDER Y_2O_3

The room temperature Raman study carried out on 99.99% optical grade powder Y_2O_3 doped with 10mol% of Eu^{3+} ions is illustrated in Figure 4.5.1. The Raman bands were characterized in cm^{-1} relative to the 457.8nm, 488.0nm, and 514.5nm excitation lines respectively. Raman shifts were observed stokes and anti-stokes to the excitation line within a ΔX= 10-1000 cm^{-1}. The positions of the Raman bands were independent of the excitation line confirming that they are due to Raman scattering and not fluorescence. As expected Raman bands were sharp and narrow since cubic phase Y_2O_3 represents an ordered system of low symmetry. G. Schaak et al. [55], determined the symmetry of the transitions observed in the crystal by transforming the scattering tensors for the different symmetry types of the group T_d from the co-ordinate system of the cubic crystals, where we should expect to observe 20 Raman-active transitions. However, most of the predicted transitions will not be observable due to unresolved factor-group splitting or to movements of groups of ions in the lattice related to a small dipole moment or small changes in polarizability [55].

From Figure 4.5.1, it was possible to isolate five Raman active transitions. As expected a broad gap was observed between 200 and 310 cm^{-1} suggesting an assignment of these lines at higher frequencies to the inner vibrations of an R.E.-O_6 octahedron [55].

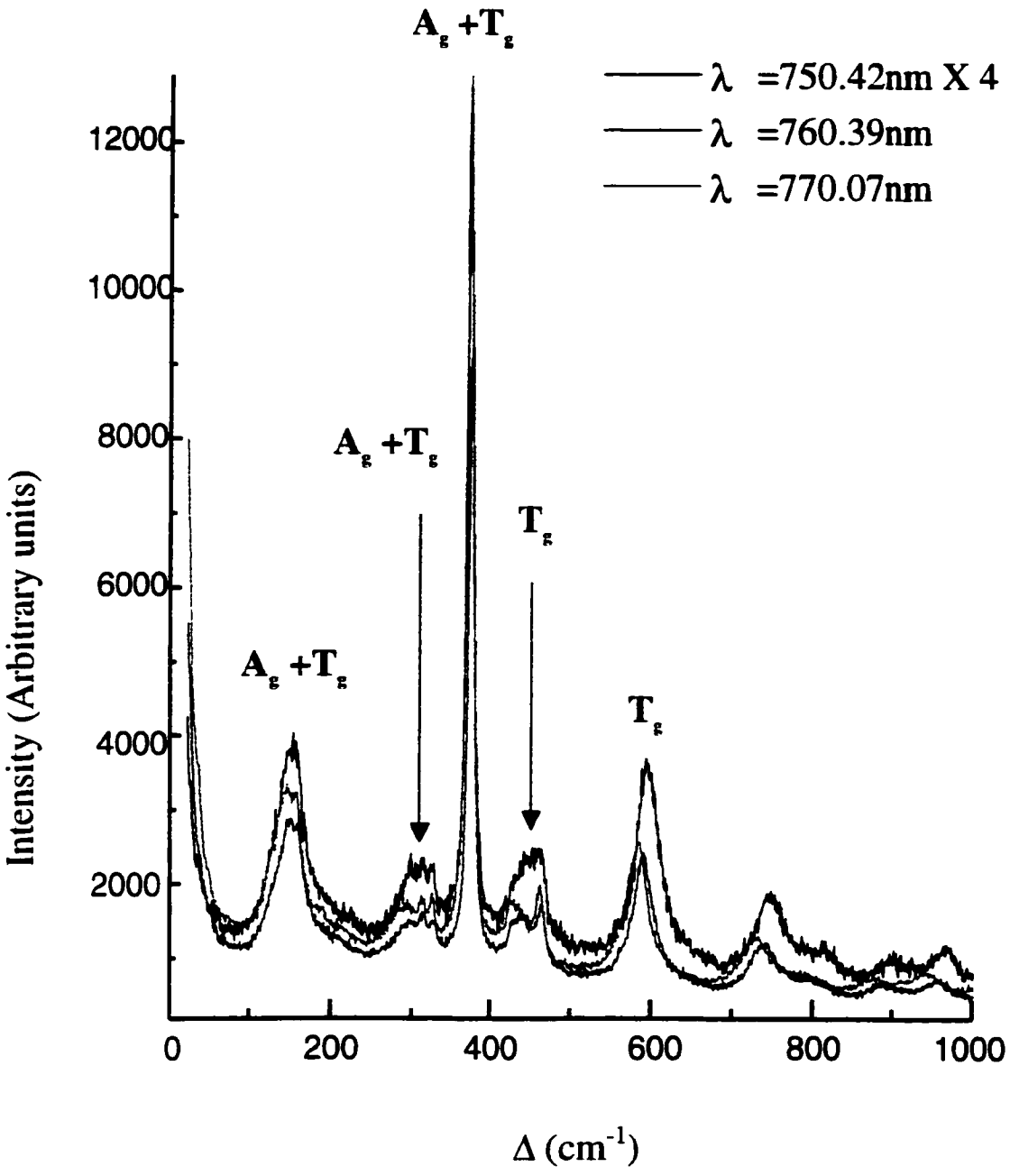

Figure 4.5.1: Room Temperature Raman Scattering of 10mol% Eu^{3+}:Y_2O_3 Bulk Sample

Figure 4.5.1 illustrates that the Raman bands observed are independent of the excitation line, where the most intense Raman transition occurred at 377 cm^{-1} of the symmetry type A_g+T_g corresponding to the totally symmetric vibration of these octahedrons [55]. Furthermore, calculations have confirmed that Raman scattering intensity of Eu^{3+} ions in a general cubic crystalline field are favored in intensity by a factor of 30 when, $\Delta J=2$ over the $\Delta J=1$ transitions. The reason behind this, is that in the free ion case, where J is a good quantum number, quadrupole scattering is forbidden for a transition where $J=0\rightarrow J=1$ but allowed for one when $J=0\rightarrow J=2$ [55]. The Raman transitions at ~160 cm^{-1} of A_g+T_g type symmetry represent the small factor-group for translational motion, which occurs below 200cm^{-1}.

Well ordered systems such as cubic phase Y_2O_3 tend to exhibit sharp Raman bands indicative of the $k = 0$ phonon modes [56]. The optically active phonons of Eu^{3+} doped Y_2O_3 can be separated into two groups; group one (above 300cm^{-1}) represents the internal vibrations of R.E.-O_6, where as the other group (below 200cm^{-1}) include the translational motions of these octahedrons and the rare earth ions [57].

Infrared lattice vibrational studies were carried out in order to distinguish between C_2-type and C_{3i}-type Raman bands, since C_{3i} sites cannot be simultaneously I.R. and Raman active due to its center of inversion [56]. From the results shown in Figure 4.5.2, it has been confirmed that the Raman bands occurring at 430, 468, and 590 cm^{-1} correspond to the C_2 site (i.e. T_g symmetry) only since they are both I.R. and Raman active. Thus, the remaining bands at 326 and 376 cm^{-1} are due to a combination of both

C_2 and C_{3i} sites (i.e. A_g + T_g symmetry). The I.R. stretches, Raman bands, symmetry assignment, and predicted transition intensities observed for the powder Y_2O_3 are presented in Table 4.5.1. The I.R. stretches for the Y_2O_3 powder correspond to those previously studied by McDevitt et al. [57].

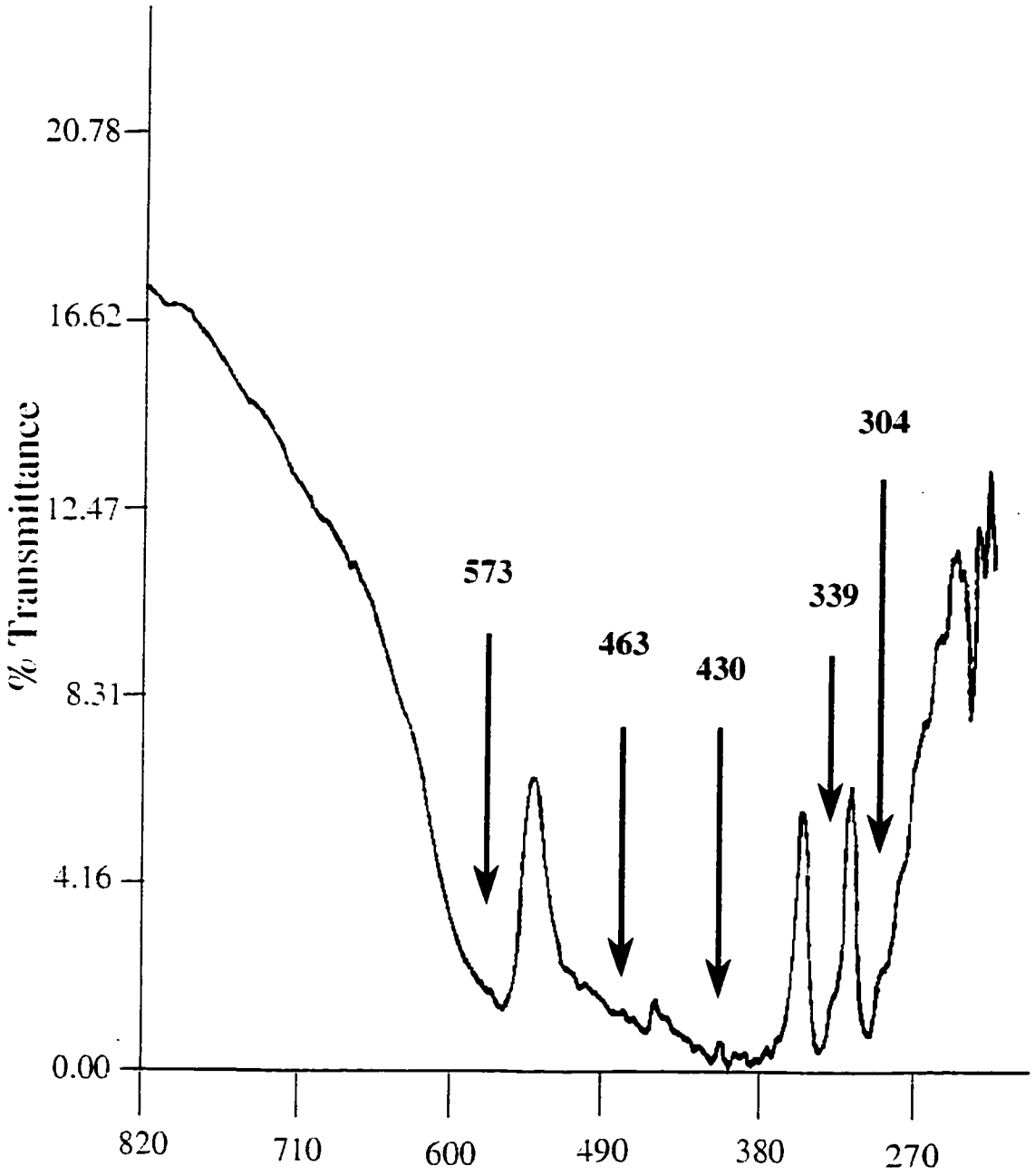

Figure 4.5.2: Room Temperature Diffuse Reflectance (FTIR) of 10mol% Eu^{3+}:Y_2O_3 Bulk Sample

Table 4.5.1: Summary of Raman Bands and I.R. Stretches of Powder Y_2O_3

[a]I.R. Stretch cm^{-1}	[b]Raman Band cm^{-1}	[c]Symmetry	[d]Predicted Intensity
304.0	326	A_g+T_g	low
338.5	376	A_g+T_g	high
430.2	*429	T_g	low
463.0	*469	T_g	medium
573.2	*590	T_g	low

*Contribution from C_2 site only, [(a)] [57], [(b)] See Figure 4.5.1. 10mol% Eu^{3+}:Y_2O_3 Bulk Sample at room temperature, [(c)] [49,55], [d)] [49].

4.6 X-RAY DIFFRACTION AND SCANNING ELECTRON MICROSCOPY OF CUBIC PHASE Y_2O_3

The particle diameters and general morphology for the nanocrystal samples were characterized via powder X-ray diffraction (XRD) and scanning electron microscopy (SEM) respectively. The particle sizes were determined from X-ray diffraction line widths using the Scherrer equation [58,59] given below:

$$D = \frac{0.9\lambda}{B_e[2\theta]\cos(\theta)} \qquad 4.6.1$$

Where $B_e(2\theta)$ represents the peak width at half height after Warren's correction equation for experimental broadening is applied as follows:

$$[B_e(2\theta)]^2 = [B_e(2\theta)]^2 - B_r(2\theta)]^2 \qquad 4.6.2$$

Where $B_e(2\theta)$ and $B_r(2\theta)$ represents the peak width at half height for the analyzed powder and for the Si standard material, respectively. For this study, commercial Y_2O_3 with 99.99% purity was compared to the samples and was found to have no line broadening. Figure 4.6.1 illustrates the X-ray diffraction patterns of commercial Y_2O_3, 1mol% Eu^{3+}:Y_2O_3 bulk and nanocrystal samples. The (222) line for the samples at ~29° (2θ) and the (111) line for Si were used to determine the average particle diameter. Thus, equations 4.6.1 and 4.6.2 yield a particle diameter of 148 Å, 208Å for the 1mol%

$Eu^{3+}:Y_2O_3$ combustion nanocrystals and hydrolysis nanocrystals. There was no detectable line broadening for the 1mol% $Eu^{3+}:Y_2O_3$ bulk sample, therefore, the exact particle size could not be measured, however, the average particle dimension was estimated to be larger than 1000 Å.

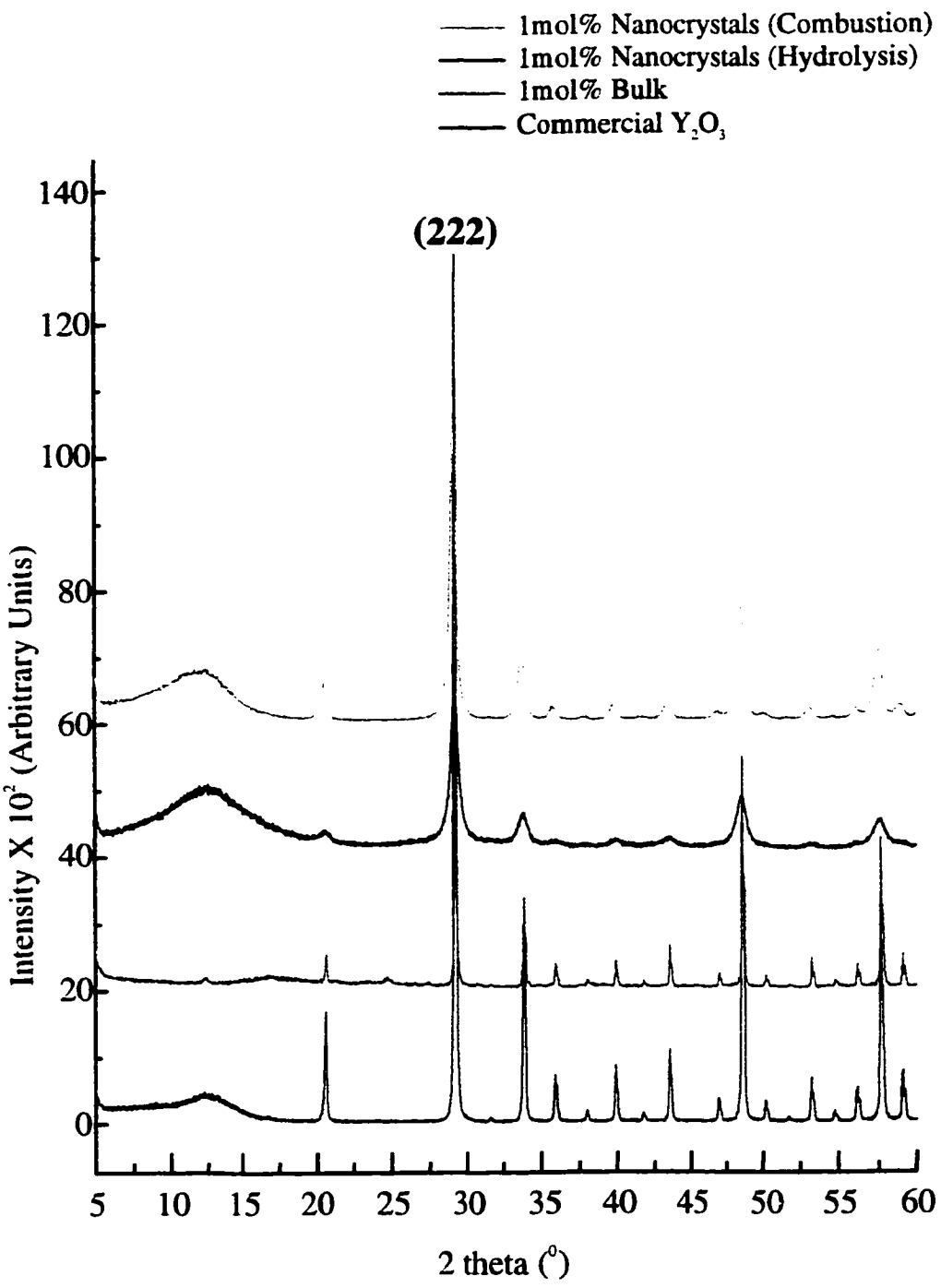

Figure 4.6.1: X-ray Diffraction Patterns of 1mol% Eu^{3+}:Y_2O_3 Samples . The (222) Peak was used to Determine the Average Particle Size

This allows one to conclude that the combustion method produces the smallest particle sizes of the three preparation methods. This confirmed that phase disorder effects at the surface of the nanocrystal particles were present since the average particle size for the sample was determined to be below 300 Å [51].

The popularity of SEM is due to its ability to provide imaging of the topographical structure of a solid surface [60]. SEM results were necessary to confirm the general morphology for the various Eu^{3+}:Y_2O_3. Magnifications up to 100X were used to study the nanocrystalline surface, which confirms the appearance of a semi-porous crystalline structure for the Y_2O_3 nanocrystalline samples in Figure 4.6.2.

As expected, the combustion sample expressed the most porosity of the three samples intrinsic to the preparation method involving glycine nitrate fueled combustion. The pores and voids shown in Figure 4.6.2 result from gases evolved during the combustion synthesis [61]. The particle sizes produced by this method are random and very difficult to control, thereby often causing phase distortion, which can affect the spectroscopy observed from such samples. Recall that in our site selective study we observed an evident red shift with the 1mol% Eu^{+}:Y_2O_3 nanocrystal combustion sample at 77K. The SEM image for the 1mol% Eu^{3+}:Y_2O_3 nanocrystal hydrolysis sample is that of a more ordered surface with less porosity than the combustion sample. The bulk sample with its large particle sizes expressed the highest surface order.

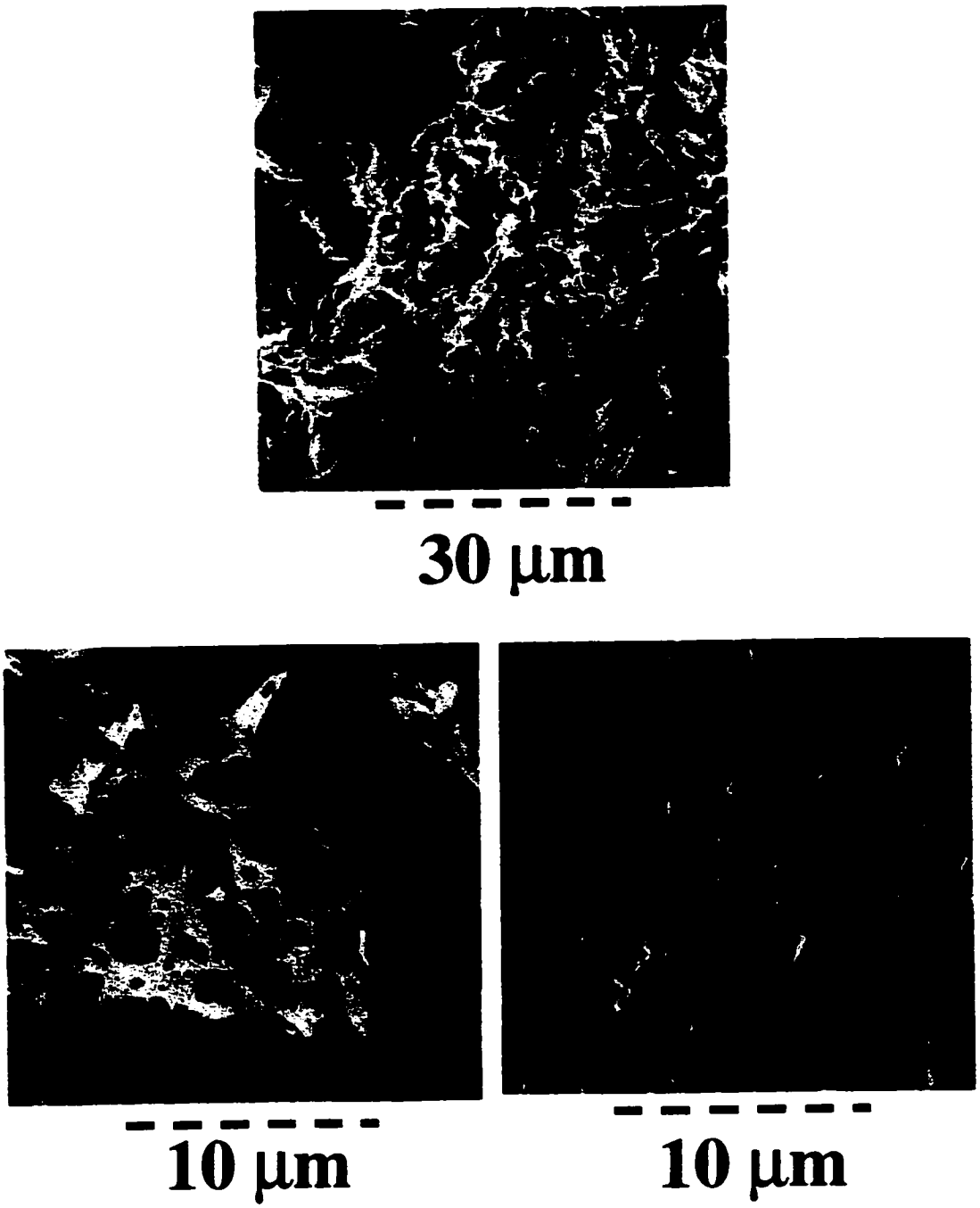

Figure 4.6.2: Scanning Electron Microscopy of 10mol% Eu^{3+}:Y_2O_3 Samples

4.7 REFERENCES

[1] Cotton A. F., Wilkinson G., Advanced Inorganic Chemistry, Interscience Publishing, New York, 1972.

[2] Zumdahl S., Chemistry 3rd Edition, D.C. Heath and Company, USA, 1993.

[3] Bethe H.A., *Ann. Phys.*, 3, 133 (1929).

[4] Kramers M.H.A., *Proc. Acad. Sci. Amsterdam*, 32, 1176 (1929).

[5] Freed S., Spedding F.H., *Nature*, 123, 525 (1929).

[6] Freed S., *Phys. Rev.*, 38, 2122 (1931).

[7] Spedding F.H., Hamlin H.F., *J.Chem. Phys.*, 5, 429 (1937).

[8] Van Vleck J.H., *J. Phys. Chem.*, 41, 67 (1937).

[9] Broer L.J.F., Gorter C.J., Hoogschagen J., *Physica*, 11. 231, (1945).

[10] Elliot R.J., Stevens K.W.H, *Proc. Roy. Soc (London) A*, 215, 437 (1952).

[11] Elliot R.J., Stevens K.W.H., *Proc. Roy. Soc (London) A*, 219, 387 (1953).

[12] Hellwege K.H., *Ann. Phys.*, 4, 95, (1948).

[13] Wayant R., Marwood E., Electro-Optics Handbook, Mc-Graw Hill Inc., USA, 1994.

[14] Alivisatos, A.P., "*Nanocrystals: Building Blocks for Modern Materials*", Endeavor, Vol. 21 (2) 1997, 56-60.

[15] Anh, K.T., Ngoc T., Nga T.P., Bich V.T., Long P., *J. Lumin.*, 39, 215-221 (1998).

[16] Bihari B., Hergen E., Tissue M. B., *J. Lumin.*, 75, 1-10 (1997).

[17] Wickersheim K.A., Lefever R.A., *J. Electrochem. Soc.*, 111, 47 (1964).

[18] Forest H., Ban G., *J. Electrochem Soc.: Solid State Science*, 29, 474-477 (1969).

[19] Williams, D.K., Bihari B., Tissue M. B., *J. Phys. Chem.*, 102, 916-920 (1998).

[20] Heber J., Hellwege K.H., Köbler U., Murmann H., *Z. Physik*, 237, 189-204 (1970).

[21] Heber J., Köbler U., Luminescence of Crystals, Molecules and Solutions ed. F., Williams Plenum Press, New York, 1973.

[22] Jagannathan R., Kutty T.R.N., Kottaisamy M., Jeyagopal P., *Jpn. J. Appl. Phys.*, 33, 6207-6212 (1994).

[23] Singh J., Excitation Energy Transfer Process in Condensed Matter, Plenum Press, New York, 1995.

[24] Förster T., *Ann. Phys.*, 2, 55 (1948).

[25] Dexter D.L., *J. Chem. Phys.*, 21, 836 (1953).

[26] Innokuti M., Hirayama, *J. Chem Phys.*, 43, 1978 (1965).

[27] Hewes R.A., Sarver J.F., Phys. Rev., 182, 427 (1969).

[28] Johnson L.F., Guggenheim H.J., Appl. Phys. Lett., 19, 44 (1971).

[29] Alivisatos N., *Appl. Phys. Lett.*, 271, 933-940 (1996).

[30] Tolbert S.H., Alivisatos N., *J. Phys. Chem.*, 46, 595 (1995).

[31] Leavitt R.P., Gruber J.B., Chang N.C., Morrison C.A., *J. Chem. Phys.*, 76, 4775-4788 (1982).

[32] Gruber J.B., Leavitt R.P., Morrison C.A., Chang N.C., *J. Chem. Phys.*, 82, 5373-5378 (1985).

[33] Hüfner S., Optical Spectra of Transparent Rare Earth Compounds, Academic Press Inc., New York, 1978.

[34] Henderson B., Imbusch G.F., Optical Spectroscopy of Inorganic Solids, Oxford Science Publications, New York, 1978.

[35] Atkins P.W., Physical Chemistry Fourth Edition, W.H. Freeman & Co., New York, 1978.

[36] Drago R.S., Physical Methods in Chemistry, W.B. Saunders Company, Philadelphia, USA, 1977.

[37] Buijs M., Meyerink A., Blasse G., *J. Lumin.*, 37, 9-20 (1987).

[38] Qiang L., Lian G., and Dongsheng Y., *NanoStruc. Mater.*, 8, 825-831 (1997).

[39] Jain K., Gupta A., *Bulletin of Mater. Sci.*, 17, 551 (1994).

[40] Wilson C., Li Y., *Nanostruc. Mater.*, 2, 391 (1993).

[41] Blasse G., Grabmaier B.C., Luminescent Materials, Springer Verlag, 1994.

[42] Bhargava R.N., *J. Lumin.*, 72, 190-195 (1996).

[43] Krupke W.F., *Phys. Rev.*, 145, 325-337 (1966).

[44] Di Bartolo B., Optical Interactions in Solids, John Wiley & Sons, New York, 1968.

[45] Hunt R.B., Pappalardo R.G., *J. Lumin.*, 34, 133-146 (1985).

[46] Tissue B.M., *Chem. Mater.*, 10, 2837-2845 (1998).

[47] Hergen E., Tissue B.M., *Chem. Phys. Lett.*, 251, 74-78 (1996).

[48] Goldburt E.T., Kulkarni B., Bhargava R.N., Taylor J., and Libera M., *J. Lumin.*, 72-74, 190 (1997).

[49] Ye T., Guiwen Z., Weiping Z., Shagda X., *Mater. Res. Bull.*, 32, 501, (1997).

[50] Tessari G., Bettinelli M., Speghini A., Ajò D., Pozza G., Depero L.E., Allieri B., Sangaletti L., *Appl. Surf. Sci.*, 144-145, 686 (1999).

[51] Li Z., Hahn H., Siegel R.W., Mater. Lett., 6, 342 (1988).

[52] Sharma P.K., Jilavi M.H., Nass R., Schmidt H., *J. Lumin.*, 82, 187-193 (1999).

[53] Weber M.J., *Phys. Rev.*, 171, 283 (1968).

[54] Shinn M.D., Sibley W.A., Drexhage M.G., Brown R.N., *Phys. Rev. B.*, 27, 6635 (1983).

[55] Schaak G., and Koningstein J.A., *J. Opt. Soc. Am.*, 60, 1110 (1970).

[56] Yashima M., Lee J.H., Kaklhana M., Yoshimura M., J. Phys. Chem. Solids, 58, 1593-1597 (1997).

[57] Mc Devitt N., Davidson A.D., *J. Opt. Soc. Am.*, 56, 636-638 (1966).

[58] Dénès G., *Carbon*, 33, 1265-1278, (1995).

[59] Dénès G., Le Van Mao R., Vaillancourt A., Mat. Res. Soc. Symp. Proc., 356, 105-110 (1995).

[60] Belk J.A., Electron Microscopy and Microanalysis of Crystalline Materials, Applied Science Publishers Ltd., London, 1979.

[61] Shea L.E., McKittrick J., Lopez O.A., *J. Am . Ceram. Soc.*, 79, 3257-3265 (1996).

CHAPTER 5

5.1 CONCLUSIONS

It has been shown using site selective spectroscopy, that Eu^{3+} ions does not express preferential occupation towards either C_2 or C_{3i} sites in both nanocrystalline and bulk samples. The 1.0mol% Eu^{3+} doped cubic Y_2O_3 samples confirmed that a two way energy transfer process occurs over a $90cm^{-1}$ energy gap between the $^5D_0$ level of the C_{3i} site to the $^5D_0$ level of the C_2 site. This process is possible through thermal bridging and has proven to be equally efficient at low temperatures. We confirmed this energy transfer process though our lifetimes studies that the decay time of the $^5D_0$ (C_2) level lengthens with C_{3i} excitation. From the spectral data obtained we were able to build and energy level scheme for the lowest manifold of the ^5D and ^7F terms since our results are in excellent agreement with the single crystal work of Heber at al. [21]. Raman and I.R. spectra were able to confirm the presence of two distinct sites as the C_{3i} sites posses a center of inversion and therefore, cannot simultaneously possess infrared and Raman active modes. The temperature dependence study confirmed a direct two-step thermalization process between the $^5D_0$ level of the C_2 and C_{3i} sites that obeyed Boltzmann distribution between 298K and 150K. Temperatures below 150K seem to affect the two-energy transfer step observed at higher temperatures thereby stabilizing the cycling effect between the $^5D_0$ levels. The energy gap determined from the slope of the logarithm of the intensity versus 1/T was $82cm^{-1}$, which is in excellent agreement with the value obtained from spectra of $90cm^{-1}$. X-ray diffraction was successful in

determining particle diameters of 148, 208 and >1000 Å for the 1mol% nanocrystal (combustion), nanocrystal (hydrolysis) and bulk sample respectively. The small particle diameter determined for the nanocrystals prepared via the combustion method confirm the probability of surface phase disorder which explains the large shift in the site selective emission associated with that sample. The small particle sizes for the nanocrystal samples is the likely cause for their blue shifting phenomena observed in their emission spectra in comparison to the bulk sample.

Thus, from the various experimental techniques employed in this study and at this stage of research, the 1mol% Eu^{3+}:Y_2O_3 nanocrystal sample prepared by the hydrolysis method seems to be an ideal candidate for producing high efficiency luminescent nanocrystals with tailored functions in the future production of optical materials.

5.2 FUTURE WORKS

The next phase of this study would involve an in-depth investigation into the exact extent of the energy transfer process between Eu^{+} in the two distinct sites. Further experiments would involve collecting excitation spectra at low temperature in order to better understand the exact energy mechanism involved at the $^5D_0$ level of either the C_2 and C_{3i} site. Once a mechanism can be confirmed for the energy transfer cross-over point determined to be 150K for the forward process, the next step would include calculating the Boltzmann distribution at both sites as this would assign a numerical value to the probability of either transition occurring.

In addition, the experimental data obtained in this study could be further supported by the incorporation of molecular modeling. Computer modeling results for the energy transfer process between the ions can now be generated as the basic foundation for the starting parameters has now been paved.